Role of Tropical SST Variability on the Formation of Subtropical Dipoles

Yushi Morioka, Sébastien Masson, Pascal Terray, Chloé Prodhomme, Swadhin K. Behera, Yukio Masumoto

Role of tropical SST variability on the formation of subtropical dipoles

Yushi Morioka[1], Sébastien Masson[2], Pascal Terray[2], Chloé Prodhomme[2], Swadhin K. Behera[1], and Yukio Masumoto[1]

[1]*Research Institute for Global Change, JAMSTEC, Yokohama, Japan*

[2]*LOCEAN-IPSL, Université Pierre et Marie Curie, Paris, France*

Journal of Climate (accepted)

Mar 7, 2014

Corresponding author address: Dr. Yushi Morioka,

Research Institute for Global Change, JAMSTEC,

3173-25, Showamachi, Kanazawa-ku, Yokohama City, Kanagawa, 236-0001, Japan.

E-mail: morioka@jamstec.go.jp

Abstract

Interannual variations of Sea Surface Temperature (SST) in the midlatitudes of the Southern Hemisphere play an important role in the rainfall variability over the surrounding countries by modulating synoptic-scale atmospheric disturbances. These are frequently associated with a northeast-southwest oriented dipole of positive and negative SST anomalies in each oceanic basin, referred to as a subtropical dipole. This study investigates the role of tropical SST variability on the generation of subtropical dipoles by conducting SST-nudging experiments using a coupled general circulation model. In the experiments where the simulated SST in each tropical basin is nudged to the climatology of the observed SST, the subtropical dipoles tend to occur as frequently as the case in which the simulated SST is allowed to freely interact with the atmosphere. It is found that without the tropical SST variability, the zonally elongated atmospheric mode in the mid-high latitudes, called the Antarctic Oscillation (AAO), becomes dominant and the stationary Rossby waves related to the AAO induce the SLP anomalies in the midlatitudes, which, in turn, generate the subtropical dipoles. These results suggest that the tropical SST variability may not be necessary for generating the subtropical dipoles, and hence provide a useful insight into the important role of the AAO in the midlatitude climate variability.

1. Introduction

More than 80 % of the surface area in the Southern Hemisphere is covered by ocean, and the ocean plays a key role in the rainfall over land as moisture sources. Many countries are located in the low-mid latitudes (0º-50ºS), and highly dependent on rain-fed agriculture. In these regions, rainfall variability is strongly linked with climate variability involving the low-mid latitude oceans, and greatly influences the crop yields, infrastructure, and drinking water (e.g. Jury 2002). A large number of studies on the rainfall variability discussed the impacts of the tropical climate variability such as El Niño-Southern Oscillation (ENSO) (Chiew et al. 1998, Grimm et al. 2000, Richard et al. 2000), but recently, much focus has been placed on links with the midlatitude ocean variability (Reason 2001, Robertson et al. 2003, Ummenhofer et al. 2009, Cai and Cowan 2013).

One of the major oceanic factors for the rainfall variability is Sea Surface Temperature (SST). The SST in the midlatitudes seasonally changes due mostly to solar radiation, and reaches its peak during austral summer (December-February). The SST also undergoes a year-to-year variability, which becomes large during austral summer because of a shallow mixed layer and high solar insolation. The interannual SST variation in the midlatitudes is frequently associated with a northeast-southwest oriented dipole of SST anomalies in each oceanic basin, referred to as a subtropical dipole. Behera and Yamagata (2001) first identified this phenomenon in the southern Indian Ocean. Since then, several studies have shown the existence of subtropical dipoles in the South Atlantic (Fauchereau et al. 2003) and South Pacific (Morioka et al. 2013b).

The generation mechanism of the subtropical dipoles has been widely discussed in the

62 literature (Suzuki et al. 2004, Hermes and Reason 2005, Chiodi and Harrison 2007, Morioka
63 et al. 2010, 2011, 2012). At the beginning, variations in the subtropical high during late
64 austral spring generate a northeast-southwest oriented dipole of latent heat flux anomalies.
65 This induces dipole anomalies of mixed-layer thickness, and modulates warming of the mixed
66 layer by shortwave radiation. This results in the dipole SST anomalies associated with the
67 subtropical dipole during austral summer. Therefore, the variation in the subtropical high is a
68 key factor for generating the subtropical dipole.

69 However, possible sources of variability in the subtropical high are not fully understood.
70 Huang and Shukla (2006, 2008) and Morioka et al. (2013a) conducted several Coupled
71 General Circulation Model (CGCM) experiments and suggested that not only ENSO but the
72 atmospheric variability in the mid-high latitudes, called the Antarctic Oscillation (AAO;
73 Thompson and Wallace 2000), may be important for inducing the variability of the Mascarene
74 High, hence generating the Indian Ocean Subtropical Dipole (IOSD). Also, in the CGCM
75 experiments by Morioka et al. (2013a), the IOSD occurs even without the SST variability
76 outside the southern Indian Ocean, suggesting a potential role of the local air-sea feedback
77 during the development of the IOSD, which was discussed by Behera and Yamagata (2001).
78 However, the CGCM used in their studies did not include a sea-ice model and there may be
79 some uncertainties in their simulation for the mid-high latitudes climate. In fact, a large
80 number of studies suggested the importance of sea-ice variability in the high-latitude
81 atmospheric variability through changes in the surface albedo and the air temperature
82 (Simmonds and Budd 1991, Hudson and Hewitson 2001, Raphael 2003).

83 As the dominant atmospheric variability in the Southern Hemisphere, the AAO plays a

84 key role in the SST, mixed-layer, and sea-ice variability in the extratropics (Sen Gupta and
85 England 2006, Ciasto and Thompson 2008, Screen 2010). Several studies discussed that the
86 AAO is an internal atmospheric variability sustained by the positive feedback between the
87 zonal-mean flow and eddies (Lorenz an Hartmann 2001, Eichelberger and Hartmann 2007).
88 The positive (negative) AAO is driven by the eddy momentum flux convergence/divergence
89 associated with a strong (weak) anticyclonic Rossby wave breaking on the equator side of the
90 midlatitude jet (Gong et al. 2010, Wang and Magnusdottir 2011). In addition, the SST
91 anomalies associated with the AAO thermodynamically affect the atmosphere in the
92 troposphere and contribute to the persistence of the AAO, suggesting an existence of
93 ocean-to-atmosphere feedback (Sen Gupta and England 2007).

94 Another important driver for the climate variability in the Southern Hemisphere is
95 atmospheric teleconnection associated with the tropical heating anomalies (Lee et al. 2009).
96 In particular, ENSO has significant impacts on the SST anomalies in the extratropics by
97 modulating surface turbulent heat flux and Ekman heat advection (Ciasto and England 2011).
98 The atmospheric response to ENSO has an equivalent barotropic dipole structure of the
99 zonal-mean wind anomalies in the mid-high latitudes and it is also related with the AAO
100 (L'Heureux and Thompson 2006).

101 In this context, a large number of studies discussed the role of the AAO and ENSO in
102 the SST variability in the extratropical Southern Hemisphere, but little attention has been paid
103 to the SST variability associated with the subtropical dipoles as well as the impacts arising
104 from the other tropical forcing. For example, the interannual SST variability in the tropical
105 Indian Ocean shows either Indian Ocean Basin (IOB; Klein et al. 1999) or Indian Ocean

106 Dipole (IOD; Saji et al. 1999) modes. Particularly, the IOD induces the atmospheric
107 teleconnection in the Southern Hemisphere (Chan et al. 2008) and plays an important role in
108 the rainfall variability over Australia (Cai et al. 2011, Cai and Rensch 2013). The Atlantic
109 Niño is another such large interannual SST variability in the tropical Atlantic (Zebiak 1993).
110 Therefore, this study aims to investigate roles of the SST variability in each tropical
111 ocean for generation of the subtropical dipoles in the Southern Hemisphere. For this purpose,
112 we perform a series of SST-nudging experiments by using a CGCM which includes a sea-ice
113 model. The contents of this paper are as follows. In Section 2, we briefly describe CGCM
114 experiments, observational data, and methodology for the atmospheric analysis. In Section 3,
115 we compare characteristics of the subtropical dipoles among the observation and the CGCM
116 experiments. In Section 4, we perform composite analysis to discuss generation of the
117 subtropical dipole among the experiments. The discussion and conclusions are given in
118 Section 5.
119
120 ## 2. Model, data, and methodology
121
122 ### 2-1. CGCM experiments
123 The CGCM used in this study is SINTEX-F2 (Masson et al. 2012). The atmospheric
124 component is ECHAM5 (Roeckner et al. 2003), which has 31 vertical levels on a T106
125 Gaussian grid. The oceanic component is NEMO (Madec 2008), which includes the LIM2
126 sea ice model (Fichefet et al. 1997) and has ORCA05 horizontal resolution (0.5º) with 31
127 vertical levels. The atmospheric and oceanic fields are exchanged every 2 hours with no flux
128 correction by means of the OASIS3 coupler (Valcke et al. 2004). For the control run (CTR)

experiment, the SINTEX-F2 is integrated for 110 years, and monthly mean outputs from the last 80 years are used for the analysis.

Using the SINTEX-F2, we conducted three SST-nudging experiments to examine the role of tropical SST variability. Details of each experiment are given in Table 1a. In the FTP experiment, the SST in the tropical Pacific (30ºS-30ºN) is nudged to climatology of the AVHRR-only Optimum Interpolation SST version 2 data (OISST v2; Reynolds et al. 2007) for the 1982-2010 period. We added a negative feedback (-2,400 W m^{-2} K^{-1}) to the surface heat flux so that the temperature in the upper 50-m mixed layer is restored within 1 day. Within 5 degrees near the boundaries of the SST-nudging area, a Gaussian smoothing is applied. Similarly, the FTIO and FTA experiments were performed in the tropical Indian and Atlantic (30ºS-30ºN) Oceans, respectively. All of these experiments are integrated for 50 years, and the monthly outputs for the last 30 years are used for the analysis by removing the first 20 years for the oceanic adjustment to the atmospheric forcing.

For an accurate interpretation of the results from the SST-nudging experiments, it should be noted that the surface heat flux correction in the SST-nudging experiments acts to inhibit coupled interactions and variability in the corrected region to a large extent. In other words, the differences between the CTR and each SST-nudging experiment may allow us to deconvolve the impact of the SST variability in each tropical basin onto the subtropical modes of the Southern Hemisphere.

2-2. Data

For comparison, we use the observed monthly mean SST data from the NOAA OISST

v2 (Reynolds et al. 2002). It has a horizontal resolution of 1° x 1° and covers the 1982-2011 period. Similar results are obtained for the different datasets such as the HadISST (Rayner et al. 2003) and ERSST v3 (Smith et al. 2008). We also use the Sea Level Pressure (SLP) and the geopotential height and horizontal winds at 250 hPa from the NCEP/DOE AMIP-II Reanalysis (Reanalysis-2; Kanamitsu et al. 2002). It covers the same period with a horizontal resolution of 2.5º x 2.5º. For precipitation, we use the observed data set from CPC Merged Analysis of Precipitation (CMAP; Xie and Arkin 1997). The resolution and analysis period are the same as in the NCEP Reanalysis-2. For all the above datasets, monthly anomalies were calculated after removing the liner trend and the monthly climatology.

2-3. Wave activity flux

We use a wave activity flux to examine propagation pathways of stationary Rossby waves on a zonally varying basic flow in the upper troposphere (Takaya and Nakamura 1997, 2001). It provides a snapshot for three-dimensional propagation of quasi-geostrophic eddies in a phase independent manner and is parallel to their local group velocity. The formulation of the wave activity flux $\vec{W}_s$ is given as follows:

$$\vec{W}_s = \frac{p}{2|\vec{U}|}\begin{pmatrix} U(\psi_x'^2 - \psi'\psi'_{xx}) + V(\psi'_x\psi'_y - \psi'\psi'_{xy}) \\ U(\psi'_x\psi'_y - \psi'\psi'_{xy}) + V(\psi_y'^2 - \psi'\psi'_{yy}) \\ \frac{f_0^2}{N^2}\left[U(\psi'_x\psi'_z - \psi'\psi'_{xz}) + V(\psi'_y\psi'_z - \psi'\psi'_{yz})\right] \end{pmatrix}, \quad (167)$$

where $p = (\text{pressure}/1000\text{hPa})$, $\vec{U} = (U,V)$ is the horizontal wind, ψ is the streamfunction, f_0 is the Coriolis parameter and N is the buoyancy frequency. Here, $(\ )'$ indicates the deviation from the monthly climatology. The divergence (convergence) of the wave activity

171 flux corresponds to the generation (dissipation) of the Rossby waves. The wave activity flux,
172 by definition, is based on the quasi-geostrophic approximation so that it is hard to describe the
173 flux near the Equator. Since the Rossby waves are excited by the vorticity perturbation
174 associated with the thermal or orographic forcing (Hoskins and Karoly 1981), here instead,
175 we have used the divergence (convergence) of the horizontal winds in the upper troposphere
176 to describe potential sources of the Rossby waves.
177

178 ## 3. Impacts on characteristics of subtropical dipoles

179 Before discussing characteristics of subtropical dipoles, it is worthwhile examining to
180 what extent the SST variances change among the CGCM experiments. Figure 1 shows the
181 standard deviation of SST anomalies during austral summer. The spatial pattern of the
182 observed SST variance is well simulated in the CTR experiment, although the simulated
183 amplitude is relatively weak. In both the observation and CTR experiment, the ENSO pattern
184 clearly appears in the tropical Pacific, and thus the SST variance is much larger than in the
185 other tropical basins. Besides in the tropical Pacific, the SST in the midlatitudes generally
186 shows a large variability compared to that in the high latitudes and this observed feature is
187 well simulated in the CTR experiment.

188 Interestingly, in the absence of tropical SST variability (FTP, FTIO, and FTA
189 experiments), the SST variances in the mid-latitudes do not largely change compared to those
190 in the CTR experiment. This suggests that the amplitude of the SST variability in the
191 midlatitudes may not be strongly influenced by the tropical SST variability. Also, in the
192 absence of the SST variability in the tropical Indian and Atlantic Oceans (FTIO and FTA

193 experiments), the SST variability in the tropical Pacific remarkably increases, suggesting that
194 the SST variability in the tropical Indian and Atlantic may act to suppress the ENSO signal in
195 the CTR experiment. This change in the tropical Pacific is consistent with some CGCM
196 studies (Dommenget et al. 2006, Santoso et al. 2012) but still in contradiction with other
197 studies (Yu et al. 2002, Wu and Kirtman 2004), which need further investigation in a future
198 study. Although the weak SST variability in the tropical Pacific of the CTR experiment, the
199 SST variability in the tropical Pacific for the FTIO and FTA experiments might be closer to
200 the observed SST variability.

201 To detect the SST variability associated with the subtropical dipoles, like previous studies
202 (Huang and Shukla 2006, Kataoka et al. 2012, Morioka et al. 2012), we performed Empirical
203 Orthogonal Function (EOF) analysis to all months of the area-weighted SST anomalies in
204 each subtropical-to-midlatitude oceanic basin. Here, we used the domain of 40ºE-110ºE and
205 15ºS-50ºS for the IOSD, 60ºW-20ºE and 15ºS-50ºS for the South Atlantic subtropical dipole
206 (SASD), and 150ºE-70ºW and 25ºS-50ºS for the South Pacific subtropical dipole (SPSD),
207 respectively.

208 The spatial patterns of EOF modes for each subtropical dipole are shown in Fig. 2, and
209 their corresponding EOF modes and explained variances are given in Tables 1b and c. All of
210 these EOF modes sufficiently separate from the neighboring EOF modes (North et al. 1982),
211 except for the IOSD in the FTP experiment where the first (20.8%) and second EOF (19.1%)
212 are close to each other. Also, it should be noted that the SST-nudging area in the CGCM
213 experiments extends to 30ºS, thus overlaps the northeastern pole of the subtropical dipoles, so
214 the IOSD is not defined in the FTIO experiment, in a similar manner for the SASD and SPSD

215 in the FTA and FTP experiments.

216 In the observation, the IOSD is detected as the second EOF mode, whereas in the CTR
217 experiment, it is captured by the first EOF mode (Table 1b). The observed
218 northeast-southwest dipole of SST anomalies is simulated in the higher latitude, and this may
219 lead to a moderately high pattern correlation at 0.44. It is found that the first EOF mode in
220 the observation shows a zonal dipole of the SST anomalies and is linked with the IOB. This
221 IOB-related mode is also detected as the second EOF mode in the CTR experiment (figure not
222 shown). Because of the difference in the EOF analyses, the explained variance of the IOSD
223 in the CTR experiment is 24.5 %, larger than that in the observation, 14.2 % (Table 1c). In
224 the FTP and FTA experiments, the IOSD is identified as the first EOF mode with the
225 explained variances similar to that in the CTR experiment. Also, the spatial patterns of the
226 EOF modes for the IOSD resemble that for the CTR experiment (Fig. 2a). This suggests that
227 the IOSD may exist independent of the SST variability in the tropical Pacific or Atlantic
228 Oceans, which will be further discussed in Section 4.

229 In contrast with the IOSD, the SASD in the observation is detected as the first EOF mode
230 (Table 1b). This mode is also captured in the CTR experiment with a high pattern correlation
231 at 0.75, although the spatial pattern of the EOF mode shows a northeast-southwest oriented
232 dipole, while in the observation, it is associated with a north-south oriented dipole (Fig. 2b).
233 Also, the SASD is identified as the first EOF mode in the FTP and FTIO experiments, and the
234 explained variances are not much different among the experiments (Table 1c). However, the
235 spatial pattern of the EOF mode in the FTP experiment slightly deforms in such a way that the
236 amplitude of the southwestern (northeastern) SST anomaly pole becomes weaker (stronger)

than that in the CTR experiment. This implies that although the SASD can develop without the SST variability in the tropical Pacific or Indian Oceans, the SST variability in the tropical Pacific may have more influences on the SASD.

Similarly as in the case of the IOSD, the SPSD in the observation is captured by the second EOF mode, which is successfully simulated in the CTR experiment (Fig. 2c, Table 1b). The pattern correlation is high at 0.76. The SPSD is also captured as the third EOF mode in the FTIO experiment and as the second EOF mode in the FTA experiment. It is found that the first EOF modes in the observation and the CGCM experiments show the SST variability related to ENSO, whereas in the FTIO experiment, the SST variability in the second EOF mode is associated with the El Niño Modoki (Ashok et al. 2007). The spatial patterns and explained variances of the SPSD are almost similar among these experiments (Fig. 2c and Table 1c). This suggests that the SST variability in the tropical Indian or Atlantic Oceans may not directly influence the occurrence of the SPSD.

The robustness of the subtropical dipoles among the experiments is further examined with regard to the occurrence frequency. Due to the lack of the reliable observations before 1980s in the Southern Hemisphere, in particular, the South Pacific (see Fig. 1 in Morioka et al. 2013b), we defined subtropical dipole events as years when the principal component of the EOF modes during austral summer exceeds 0.8 standard deviation. The list of event years defined in the observation is given in Table 2, and the occurrence frequency of the total positive and negative events are summarized in Table 3. It should be noted that to compare the occurrence frequency in the CTR experiment with those in the sensitivity experiments, the standard deviation is estimated for occurrence frequencies of the 50 different sets of 30-yr

outputs in the CTR experiment. The observed occurrence frequency of the IOSD is 48.3 %, whereas in the CTR experiment, the IOSD occurs at 50.6 % close to the observation. Interestingly, the occurrence frequencies in the FTP and FTA experiments do not largely differ from that in the CTR experiment, suggesting that the interannual SST variability associated with the IOSD may not be influenced by the tropical SST variability. Similarly, the occurrence frequencies of the SASD and SPSD in the sensitivity experiments do not largely change compared to that in the CTR experiment, although the FTP experiment in the SASD shows a slight increase in the occurrence frequency.

Another important characteristic of the subtropical dipoles is a strong seasonal dependence in such a way that the SST anomalies associated with the subtropical dipoles develop during austral summer. Here, we calculated a standard deviation of principal components of the EOF modes for each month (Fig. 3). Note that the standard deviation for the 50 different sets of 30-yr outputs in the CTR experiment is also estimated. The IOSD in the observation develops from late austral spring and reaches its peak during austral summer (Fig. 3a). Although there are slight differences in the peak month of the IOSD, all CGCM experiments reasonably simulate the strong seasonality in austral summer with comparable amplitudes. Also, both the SASD and the SPSD clearly show a strong seasonality in austral summer (Figs. 3b and c), but for the SASD, there exists a large difference in the peak month and amplitude among the observation and the CGCM experiments. It is found that the difference in the SST climatology between the observation and the model simulation is much larger in the South Atlantic than in the other oceanic basins (figure not shown). This may have a link with the large disparity in its standard deviation (Fig. 3b). These results suggest

281 that the seasonal phase-locking nature of the subtropical dipoles may not be largely affected
282 by the SST variability in the other tropical oceans.
283
284 ## 4. Potential sources for the generation of subtropical dipoles
285 The above intriguing results about key characteristics of the subtropical dipoles motivate
286 us to further examine the generation of subtropical dipoles with a focus on the variations in
287 the subtropical highs. We conduct a composite analysis and discuss only the case for the
288 positive events, because the physical mechanism and its impact on the rainfall in surrounding
289 countries for the negative events is found to be almost similar but opposite to that for the
290 positive events.
291
292 ### 4-1. Indian Ocean subtropical dipole (IOSD)
293 Figure 4a shows composite SST anomalies during austral summer of the positive IOSD.
294 Here we used the same criteria for definition of the positive IOSD events as discussed in
295 Section 3, and composited 8, 20, 8, and 6 positive events for the observation, and the CTR,
296 FTP, and FTA experiments, respectively. The SST anomalies in the observation and the CTR
297 experiment show a northeast-southwest oriented dipole in the southern Indian Ocean. In the
298 tropical Pacific, the simulated SST anomalies are associated with a strong La Niña, although
299 they are not significant in the observation. The link with La Niña in the CTR experiment is
300 also seen in the FTA experiment. However, in the FTP experiment, the dipole SST anomalies
301 associated with the IOSD exist without the SST variability in the tropical Pacific. Moreover,
302 the dipole SST anomalies in the FTP experiment resemble those in the CTR experiment,

303 indicating that ENSO may not be necessarily responsible for the occurrence of the IOSD as in
304 the observation, despite of the overemphasized ENSO in the CTR experiment.

305 Since the dipole SST anomalies during the IOSD are closely linked with the SLP
306 anomalies (Behera and Yamagata 2001), we examine composite SLP anomalies in Fig. 4b.
307 Note that the SLP anomalies are calculated for Nov. (0) - Jan. (1) because of the delayed
308 oceanic response to the atmospheric forcing (Fauchereau et al. 2003). In the reanalysis data,
309 the Mascarene High anomalously strengthens, whereas in the CTR experiment, the
310 strengthening of the Mascarene High occurs in the southern part of its mean state (~30ºS)
311 during austral summer of the analysis period, indicating anomalous southward shift of the
312 Mascarene High. In the CTR experiment, the positive SLP anomalies are zonally elongated
313 in the mid-latitudes and are associated with the negative SLP anomalies over Antarctica,
314 suggesting a possible link with the positive AAO. The negative SST anomaly in the tropical
315 Indian Ocean may act to weaken the Hadley Cell and cause the negative SLP anomalies in the
316 subtropical region, but this cannot explain the positive SLP anomalies in the southern Indian
317 Ocean. Although not visible in the reanalysis data, the potential link with the AAO in the
318 CTR experiment is also found in the FTP and FTA experiments, but the zonal elongation of
319 the positive and negative SLP anomalies is much clearer in the FTP experiment.

320 In order to determine whether the stronger relationship with ENSO and the AAO in the
321 CTR experiment is due to model bias in simulating the variability inside or outside the
322 southern Indian Ocean, the model results have been further projected onto the observed EOF
323 pattern in Fig. 2a, and the resulting time series have been used as an alternative index for the
324 IOSD to compute composites in the model experiments. As expected, the derived SST

anomalies in the CTR experiment compare favorably to the observed ones in the southern Indian Ocean (figure not shown). However, the main differences in the SST and SLP anomalies between the observation and the CTR experiment still remain, especially for the stronger relationship with ENSO and the AAO. This clearly suggests that origins of the biases are probably linked to the overemphasized ENSO and the AAO, not to the fact that the simulated EOF pattern for the IOSD in Fig. 2a is different from the observed one.

To further assess the link with the AAO in the model experiments, we defined the AAO by using the geopotential height in the upper troposphere and calculated the correlation coefficient between the IOSD and the AAO. The first EOF mode of the geopotential height anomalies at 250 hPa in the reanalysis data and the CGCM experiments are associated with zonal circular positive anomalies in the midlatitudes and the negative anomalies over Antarctica, representing the AAO (Fig. 5). The variance explained by the first EOF mode in the CTR experiment (14.0 %) is very close to that in the reanalysis data (15.0 %). The correlation coefficient between the time series of the principal component of the corresponding EOF mode for the AAO during Nov.-Jan. and that for the IOSD during Dec.-Feb. is found to be significantly large at 0.45 in the CTR experiment, although not significant in the reanalysis data (Table 4). As expected, both the FTP and FTA experiments show a significantly high correlation with the AAO, and in particular, the FTP experiment shows higher correlation (0.72) than that in the CTR experiment. The comparison of the CTR and FTP experiments implies that, without the SST variability in the tropical Pacific, the AAO may play more important role in inducing the IOSD (Hermes and Reason 2005, Morioka et al. 2013a).

To investigate a physical link with the AAO in the model experiments, we calculated composite anomalies of geopotential height at 250 hPa and wave activity flux during Nov.(0)-Jan.(1) (Fig. 6a). Positive geopotential height anomalies in the southern Indian Ocean are located above the positive SLP anomalies in the reanalysis data and the CTR experiment, representing an equivalent barotropic structure in the troposphere. In the CTR experiment, the positive anomalies are zonally elongated in the midlatitudes and associated with a propagation of stationary Rossby waves from the negative anomalies over Antarctica, suggesting the physical connection with the AAO. A similar feature is also found in the FTP and FTA experiments.

To reveal potential sources of the stationary Rossby waves, we analyzed composite anomalies of the velocity potential and divergent winds at 250 hPa and the rainfall during Nov.(0)-Jan.(1) in Figs. 6b, and 7. Both the reanalysis data and the CTR experiment show an anomalous wind divergence west of the Antarctic Peninsula, but there is a large disparity in the western tropical Pacific. In the CTR experiment, anomalous divergence occurs in association with La Niña when the seasonal rainfall enhances in the western tropical Pacific (Fig. 7). The associated diabatic heating acts to generate the Rossby waves propagating along the great circle, generating the Pacific-South American (PSA; Mo and Paegle 2001) like teleconnection pattern in the South Pacific. The anomalous rainfall increase is also found over adjacent countries in the southern Indian Ocean, in particular, southern Africa in the CTR experiment, although not significant in the observation. This may be due to the anomalous moisture supply from the southern Indian Ocean linked with the westward extension of the anomalous Mascarene High (Fig. 4b). On the other hand, the rainfall

increase in Australia may be more related to La Niña in the tropical Pacific.

A similar feature of the wind divergence anomalies can be seen in the FTA experiment associated with the increased rainfall in the western tropical Pacific (Fig. 7). However, in the FTP experiment, the spatial pattern of the wind divergence anomalies resembles that in the reanalysis data (Fig. 6b), except that the anomalous divergence occurs in the tropical Indian Ocean in association with the enhanced rainfall in the region (Fig. 7). A comparison of the reanalysis and the FTP experiment suggests that without the SST variability in the tropical Pacific and associated interferences, the anomalous wind divergences in the upper troposphere of mid-high latitudes may excite the stationary Rossby waves and induce the AAO-related positive SLP anomalies in the southern Indian Ocean.

4-2. South Atlantic subtropical dipole (SASD)

The physical mechanism for the SASD is found to be almost similar to that for the IOSD. Similarly as in the IOSD, we conducted the composite analysis and used 6, 21, 9, and 7 positive events for the observation, and the CTR, FTP, and FTIO experiments, respectively. Composite SST anomalies in the observation and the CTR experiment show a northeast-southwest oriented dipole in the South Atlantic (Fig. 8a). These are associated with the negative SST anomalies in the central tropical Pacific related to La Niña. On the other hand, in the FTP experiment, the dipole SST anomaly pattern slightly deforms in such a way that the northeastern pole of the negative SST anomaly extends to the southwest of South Africa. This is expected from the spatial pattern of the corresponding EOF mode in Fig. 2b. Also, in the FTP and FTIO experiments, the SST anomalies in the tropical Pacific show no

391 significant signal, implying that ENSO may not be a necessary condition for generating the
392 SASD.

393 Similarly as in the IOSD, St. Helena High in the reanalysis data and the CTR experiment
394 anomalously strengthens in its southern part of the mean state (~30ºS) during austral summer
395 of the analysis period, indicating anomalous southward shift of St. Helena High (Fig. 8b).
396 The positive SLP anomalies do not appear to be directly linked with the SST variability in the
397 tropical Atlantic, because the negative SST anomalies in the region tend to weaken the
398 Hadley Cell and cause the negative SLP anomalies in the subtropical region. Rather, they are
399 associated with the negative (positive) SLP anomalies in the western (eastern) tropical Pacific
400 related to La Niña. Also, over Antarctica, the negative SLP anomalies dominate, indicating a
401 possible link with the positive AAO. On the other hand, the link with the positive AAO is not
402 visible in the FTP and FTIO experiments. In fact, the correlation coefficients between the
403 AAO and the SASD in the reanalysis data and the CTR experiment are significantly high, but
404 those in the FTP and FTIO experiment are not significant (Table 4). This implies that in both
405 FTP and FTIO experiments, there may exist some internal atmospheric processes responsible
406 for generating the positive SLP anomalies in the South Atlantic.

407 To reveal the physical mechanism on the positive SLP anomalies during the positive
408 SASD, composite anomalies of the geopotential height and wave activity flux at 250 hPa are
409 shown in Fig. 9a. In the reanalysis data, the positive geopotential height anomalies in the
410 South Atlantic are associated with a clear propagation of stationary Rossby waves from the
411 positive anomalies in the South Pacific through the negative anomalies west of the Antarctic
412 Peninsula. A similar propagation of the Rossby waves is found in the CTR experiment.

413 However, in the FTP experiment, the positive anomalies in the South Atlantic are associated
414 with a propagation of the Rossby waves from the positive anomalies west of Antarctic
415 Peninsula through the negative anomalies over the southern South America. Also, in the
416 FTIO experiment, the positive anomalies in the South Atlantic are associated with the
417 negative anomalies west of Antarctic Peninsula. These suggest that the atmospheric
418 variability west of Antarctic Peninsula may have influence on the positive anomalies in the
419 South Atlantic through the Rossby wave propagation, although no significant link with the
420 AAO is found in the FTP and FTIO experiments.

421 For potential sources of the stationary Rossby waves, composite anomalies of the
422 velocity potential and divergent winds at 250 hPa in the reanalysis data and the CTR
423 experiment show anomalous wind divergence near the Maritime Continent and New Zealand
424 as well as the Antarctic Peninsula (Fig. 9b). In particular, the anomalous wind divergences
425 over the Maritime Continent are related to the enhanced rainfall associated with La Niña (Fig.
426 10). The significant rainfall increase is also found over southeast Brazil both in the
427 observation and the CTR experiment, which may be partly related to the strengthening of the
428 St. Helena High supplying more moisture from the South Atlantic (Fig. 8b). Although the
429 spatial patterns of the wind divergence anomalies in the FTP and FTIO experiments resemble
430 that in the CTR experiment, there is a clear difference in the wind divergence anomalies in the
431 midlatitudes. Therefore, in the absence of the SST variability in the tropical Pacific or Indian
432 Oceans, the anomalous wind divergences in the midlatitudes may act to generate the
433 stationary Rossby waves, hence the positive SLP anomalies in the South Atlantic.

434 Finally, a strong coherence between the SASD and the IOSD is found in the analyzed

435 results. This intriguing aspect was discussed by Hermes and Reason (2005), suggesting that
436 they are highly correlated under the large-scale atmospheric forcing related to the AAO. In
437 the reanalysis data and the CTR experiment (Figs. 8b and 9a), the stationary Rossby waves
438 clearly propagate from the positive SLP anomalies in the South Atlantic through the negative
439 SLP anomalies over Antarctica to the positive SLP anomalies in the southern Indian Ocean.
440 This suggests that the atmospheric Rossby waves play an important role in physically
441 connecting the SLP anomalies, hence the subtropical dipoles in the two oceans. However,
442 some exceptions are found when some of the IOSDs occur independent of the SASDs and
443 some of the positive SASDs occur in association with the negative IOSDs and vice versa. In
444 these cases, the atmospheric signal related to the AAO is absent and less prominent than the
445 above coherent cases (Hermes and Reason 2005). This may be related to the non-linear
446 behavior of the mid-high latitude atmosphere.
447

448 ## 4-3. South Pacific subtropical dipole (SPSD)

449 The physical mechanism on the generation of the SPSD is found not to largely differ
450 from the IOSD and the SASD. Similarly, we performed composite analysis to 7, 18, 9, and 7
451 positive events for the observation, and the CTR, FTIO, and FTA experiments, respectively.
452 The positive SPSDs in the observation and the CTR experiment show slightly east-west
453 oriented dipole of positive and negative SST anomalies in the central South Pacific (Fig. 11a).
454 These are associated with the negative SST anomalies southeast of Australia and the positive
455 SST anomalies west of South America. Interestingly, both the observation and the CTR
456 experiment show an association with La Niña in the tropical Pacific. The similar dipole SST

457 anomaly is found in the FTIO and FTA experiments, but in the FTA experiment, the SST
458 anomaly in the tropical Pacific is associated with El Niño in the central tropical Pacific. This
459 implies that a phase of ENSO may have nothing to do with the occurrence of the SPSD.

460 Composite SLP anomalies in the reanalysis data and the CTR experiment (Fig. 11b) show
461 a wave train of positive and negative SLP anomalies in the central South Pacific, as discussed
462 in Morioka et al. (2013b). The wave train of the SLP anomalies does not seem to be directly
463 linked with the negative SST anomaly in the tropical Pacific, because it acts to cause
464 weakening of the Hadley Cell and hence the negative SLP anomalies in the subtropical region.
465 Rather, associated with the La Niña condition, both the reanalysis and the CTR experiment
466 show positive (negative) SLP anomalies in the eastern (western) tropical Pacific. On the
467 other hand, in the FTIO and FTA experiments, the wave train of the SLP anomalies is
468 associated with the negative SLP anomalies in the midlatitudes and the positive SLP
469 anomalies over Antarctica, indicating a possible link with the negative AAO. Although the
470 correlation coefficients between the SPSD and the AAO are not significant in the reanalysis
471 data and the CTR experiment, they are significantly negative in the FTIO and FTA
472 experiments.

473 In the upper troposphere, both the reanalysis data and the CTR experiment clearly show a
474 wave train of positive and negative geopotential height anomalies in the South Pacific (Fig.
475 12a). They are associated with a propagation of stationary Rossby waves from negative
476 anomalies southeast of Australia, which are partly related to the wave propagation from the
477 negative anomalies in the southern Indian Ocean through the positive anomalies over
478 Antarctica. A similar wave propagation is found in the FTA and FTIO experiments, but the

479 Rossby waves propagate between the negative anomalies in the midlatitudes and the positive
480 anomalies over Antarctica, indicating a strong connection with the negative AAO.

481 One of the potential sources of the stationary Rossby waves in the reanalysis data and the
482 CTR experiment may be the anomalous wind divergence in the western tropical Pacific (Fig.
483 12b). This wind divergence anomaly, although not significant, is related to the enhanced
484 rainfall over the Maritime Continent associated with La Niña (Fig. 13). Another possible
485 source may be the anomalous wind divergence in the southern Indian Ocean for the reanalysis
486 data, as discussed by Morioka et al. (2013b). On the other hand, in the FTIO experiment,
487 anomalous wind divergences significantly occur southwest of Australia as well as in the
488 tropical Indian Ocean, which are related to the anomalous rainfall increase in the southern
489 tropical Indian Ocean (Fig. 13). Since the SST variability is suppressed in the tropical Indian
490 Ocean, the enhanced rainfall may be due to an internal atmospheric variability in the tropical
491 basin. Also, in the FTA experiment, the wind divergence anomaly is found in the central
492 tropical Pacific related to El Niño and also south of South Africa (Fig. 12b). These results
493 suggest that even without the SST variability in the tropical Indian or Atlantic Oceans,
494 anomalous wind divergences in the midlatitudes may act to induce the stationary Rossby
495 waves, hence generate the wave train of the positive and negative SLP anomalies in the South
496 Pacific.

497

498 **5. Summary and discussion**

499 The role of tropical SST variability in the generation of subtropical dipoles is
500 investigated by conducting a series of CGCM experiments in the tropical oceans and the

501 results for each subtropical dipole are summarized in the schematic diagram (Fig. 14). The
502 CGCM reasonably reproduces the northeast-southwest oriented dipole of positive and
503 negative SST anomalies associated with the subtropical dipole in each oceanic basin, although
504 there exist some discrepancies for the IOSD due to the overemphasized ENSO and the AAO
505 in the model. In the experiments where the SST variability in each tropical basin is
506 suppressed by nudging the simulated SST to the observed climatology, the subtropical dipoles
507 in each oceanic basin are found to develop in association with the variations in the subtropical
508 highs. Interestingly, the occurrence frequencies of subtropical dipoles as well as their strong
509 seasonality in austral summer do not largely change in most cases of the CGCM experiments.
510 Composite analysis reveals that in the absence of the tropical SST variability, the IOSD and
511 the SPSD are associated with the AAO, whereas the SASD is associated with a wave train of
512 SLP anomalies in the midlatitudes. It is found that the Rossby waves generated in the
513 midlatitudes play an important role in inducing the SLP anomalies, hence generating the
514 subtropical dipoles. The results for the IOSD are consistent with the previous CGCM study
515 by Morioka et al. (2013a), although the link with the AAO is not significant in the composite
516 fields of reanalysis data (Table 4) and our model has a tendency to simulate the IOSD in
517 association with the AAO.

518 The most intriguing result in this study is that, when the tropical SST variability is
519 suppressed, the AAO plays an important role in the atmospheric variability of the midlatitudes,
520 and is able to induce the SST variability associated with the subtropical dipoles. The
521 extratropical SST response to the AAO and/or ENSO has been widely discussed in the
522 previous literature (Sen Gupta and England 2006, Ciasto and Thompson 2008, Ciasto and

England 2011), but few studies paid attention to the SST variability associated with subtropical dipoles and examined the relative contribution from the AAO and the tropical SST variability to the generation of subtropical dipoles. Our CGCM results suggest that the tropical SST variability acts to suppress or counteract the AAO activity inherently existing in mid-high latitudes. This tendency is clearly seen in the standard deviation of the geopotential height anomalies at 250 hPa during Nov.-Jan. (Fig. 15a). Both the reanalysis data and the CTR experiment show large interannual variations in the mid-high latitudes, which are closely linked with the AAO. Interestingly, the standard deviation over the Antarctica in the FTP and FTA experiments becomes larger than that in the CTR experiment. However, in the FTIO experiment, the amplitude of the standard deviation does not largely change compared to the CTR experiment.

Since the atmospheric variability in the upper troposphere of the mid-high latitudes is also influenced by the atmospheric teleconnection through the rainfall variability induced by the SST variability in the tropical oceans (Cai et al. 2011, Ding et al. 2012), we calculated the standard deviation of the rainfall anomalies in the same season (Fig. 15b). Both the observation and CTR experiment show large rainfall variability in the western tropical Pacific and to a lesser extent in the tropical Indian Ocean. The rainfall variability in these regions is suppressed in the FTP and FTA experiments, but does not largely change in the FTIO experiment. This implies that the atmospheric teleconnection from the western tropical Pacific and the tropical Indian Oceans becomes weaker in the FTP and FTA experiments, and the AAO becomes able to play a major role in the SLP variations of the mid-high latitudes. The difference in the rainfall variability in the experiments may be due to the basin

interactions through the change in the walker circulation related to that in the SST variability (Saravanan and Chang 2000), but this is beyond the scope of this study.

Finally, this study provides much implication for both simulation and prediction of subtropical dipoles. To realistically simulate and accurately predict the subtropical dipoles, it is necessary to represent the AAO signal in the model at least in one season prior to the occurrence of the subtropical dipoles. A previous study by Yuan et al. (2013) suggests that it is difficult to predict the subtropical dipoles that are not associated with ENSO. The AAO, itself, is the internal atmospheric variability sustained by the eddy-mean interaction and exists even without the SST variability (Yamazaki and Shinya 1999, Limpasuvan and Hartmann 1999). However, some studies claim an important role of ocean-to-atmosphere feedback in the AAO (Sen Gupta and England 2007), which is worthwhile to examine in the further CGCM study. In addition, there are external factors such as ozone influencing the AAO activity (Sexton 2001), which are not taken into account in the present study. For the realistic simulation of the AAO and hence the subtropical dipoles, it is necessary to reproduce at least both the oceanic and atmospheric mean states in the mid-high latitudes such as the SST, sea-ice, and westerly jet. In this regard, many efforts are required for realistic simulation and accurate prediction of the AAO to represent the climate variability in the midlatitudes of the Southern Hemisphere.

Acknowledgments

The SINTEX-F2 experiments were performed using HPC resources from GENCI-IDRIS (Grant 2012-x2012016895). We are grateful to three anonymous reviewers

567 for providing helpful comments and suggestions on our original manuscript. Also,
568 constructive comments from Drs. Toshio Yamagata, Jérôme Vialard, Takeshi Izumo, Hugo
569 Dayan, and J. V. Ratnam help improve the manuscript. The first author is supported by a
570 research fellowship from the Japan Society for the Promotion of Science (JSPS).
571

572 **References**

573 Ashok, K., S. K. Behera, S. A. Rao, H. Weng, and T. Yamagata, 2007: El Niño Modoki and
574 its possible teleconnection. *J. Geophys. Res.*, **112**, C11007, doi:
575 10.1029/2006JC003798

576 Behera, S. K., and T. Yamagata, 2001: Subtropical SST dipole events in the southern Indian
577 Ocean. *Geophys. Res. Lett.*, **28**, 327-330.

578 Cai, W., P. V. Rensch, T. Cowan, H. H. Hendon, 2011: Teleconnection pathways of ENSO
579 and the IOD and the mechanisms for impacts on Australian rainfall. *J. Climate*, **24**,
580 3910-3923, doi: 10.1175/2011JCLI4129.1.

581 Cai, W., and T. Cowan, 2013: Southeast Australia autumn rainfall reduction: a
582 climate-change-induced poleward shift of ocean-atmosphere circulation. *J. Climate*, **26**,
583 189-205, doi: 10.1175/JCLI-D-12-00035.1.

584 Cai, W., and P. V. Rensch, 2013: Austral summer teleconnections of Indo-Pacific variability:
585 their nonlinearity and impacts on Australian climate. *J. Climate*, **26**, 2796-2810, doi:
586 10.1175/JCLI-D-12-00458.1.

587 Chan, S. C., S. K. Behera, and T. Yamagata, 2008: Indian Ocean Dipole influence on South
588 American rainfall. *Geophys. Res. Lett.*, **35**, L14S12, doi:10.1029/2008GL034204.

589 Chiodi, A. M., and D. E. Harrison, 2007: Mechanisms of summertime subtropical southern
590 Indian Ocean sea surface temperature variability: on the importance of humidity
591 anomalies and the meridional advection of water vapor. *J. Climate*, **20**, 4835-4852,
592 doi: 10.1175/JCLI4271.1.

593 Chiew, F. H. S., T. C. Piechota, J. A. Dracup, and T. A. McMahon, 1998: El Nino/Southern

Oscillation and Australian rainfall, streamflow and drought: Links and potential for forecasting. *J. Hydrology*, **204**, 138-149.

Ciasto, L. M., and D. W. J. Thompson, 2008: Observations of large-scale ocean-atmosphere interaction in the Southern Hemisphere. *J. Climate*, **21**, 1244-1259, doi: 10.1175/2007JCLI1809.1.

Ciasto, L. M., and M. H. England, 2011: Observed ENSO teleconnections to Southern Ocean SST anomalies diagnosed from a surface mixed layer heat budget. *Geophys. Res. Lett.*, **38**, L09701, doi:10.1029/2011GL046895.

Ding, Q., E. J. Steig, D. S. Battisti, and J. M. Wallace, 2012: Influence of the tropics on the Southern Annular Mode. *J. Climate*, **25**, 6330-6348, doi: 10.1175/JCLI-D-11-00523.1.

Dommenget, D., V. Semenov, and M. Latif, 2006: Impacts of the tropical Indian and Atlantic Oceans on ENSO. *Geophys. Res. Lett.*, **33**, L11701, doi: 10.1029/2006GL025871.

Eichelberger, S. J., and D. L. Hartmann, 2007: Zonal jet structure and the leading mode of variability, *J. Climate*, **20**, 5149-5163, doi: 10.1175/JCLI4279.1.

Fauchereau, N., S. Trzaska, Y. Richard, P. Roucou, and P. Camberlin, 2003: Sea-surface temperature co-variability in the southern Atlantic and Indian Oceans and its connection with the atmospheric circulation in the Southern Hemisphere. *Int. J. Climatol.*, **23**, 663-677, doi: 10.1002/joc.905.

Fichefet, T., M. A. Morales Maqueda, 1997: Sensitivity of a global sea ice model to the treatment of ice thermodynamics and dynamics. *J. Geophys. Res.*, **102**, C6, 12609-12646.

Gong, T., S. B. Feldstein, and D. Luo, 2010: The impact of ENSO on wave breaking and

616 Southern Annular Mode events. *J. Atmos. Sci.*, **67**, 2854-2870, doi:
617 10.1175/2010JAS3311.1.
618 Grimm, A. M., V. R. Barros, and M. E. Doyle, 2000: Climate variability in the southern South
619 America associated with El Niño and La Niña Events. *J. Climate*, **13**, 35-58.
620 Hermes, J. C., and C. J. C. Reason, 2005: Ocean model diagnosis of interannual coevolving
621 SST variability in the South Indian and South Atlantic Oceans. *J. Climate*, **18**,
622 2864-2882.
623 Hoskins, B. J., and D. J. Karoly, 1981: The steady linear response of a spherical atmosphere
624 to thermal and orographic forcing. *J. Atmos. Sci.*, **38**, 1179-1196.
625 Huang, B., and J. Shukla, 2006: Interannual SST variability in the southern subtropical and
626 extratropical ocean. *COLA Tech. Rep.*, **223**, 20pp.
627 Huang, B., and J. Shukla, 2008: Interannual variability of the South Indian Ocean in
628 observations and a coupled model. *Indian Journal of Marine Sciences*, **37**, 13-34.
629 Hudson, D. A., and B. C. Hewitson, 2001: The atmospheric response to a reduction in
630 summer Arctic sea-ice extent. *Clim. Res.*, **16**, 79-99.
631 Jury, M. R., 2002: Economic impacts of climate variability in South Africa and development
632 of resource prediction models. *J. Appl. Meteor.*, **41**, 46-55.
633 Kanamitsu, M., W. Ebisuzaki, J. Woollen, S. K. Yang, J. J. Hnilo, M. Fiorino, and G. L.
634 Potter, 2002: NCEP-DOE AMIP-II Reanalysis (R-2). *Bull. Amer. Meteor. Soc.*, **83**,
635 1631-1643, doi: 10.1175/BAMS-83-11-1631.
636 Kataoka, T., T. Tozuka, Y. Masumoto, and T. Yamagata, 2012: The Indian Ocean subtropical
637 dipole mode simulated in the CMIP3 models. *Clim. Dyn.*, **39**, 1385-1399, doi:

638 10.1007s/00382-011-1271-2.
639 Klein, S. A., B. J. Soden, and N.-C. Lau, 1999: Remote sea surface temperature variations
640 during ENSO: evidence for a tropical atmosphere bridge. *J. Climate*, **12**, 917-932.
641 Lee, S. K., C. Wang, and B. E. Mapes, 2009: A simple atmospheric model of the local and
642 teleconnection responses to tropical heating anomalies. *J. Climate*, **22**, 272-284, doi:
643 10.1175/2008JCLI2303.1.
644 L'Heureux, M. L., and D. W. J. Thompson, 2006: Observed relationships between the El
645 Niño-Southern Oscillation and the extratropical zonal-mean circulation. *J. Climate*, **19**,
646 276-287.
647 Limpasuvan, V., and D. L. Hartmann, 1999: Eddies and the annular modes of climate
648 variability. *Geophys. Res. Lett.*, **26**, 3133-3136.
649 Lorenz, D. J., and D. L. Hartmann, 2001: Eddy-zonal flow feedback in the Southern
650 Hemisphere. *J. Atmos. Sci.*, **58**, 3312-3327.
651 Madec, G., 2008: NEMO ocean engine, *Note du Pôle de Modélisation*, Institut Pierre-Simon
652 Laplace (IPSL), France, No 27. ISSN No 1288-1619.
653 Masson, S., P. Terray, G. Madec, J. J. Luo, T. Yamagata, and K. Takahashi, 2012: Impact of
654 intra-daily SST variability on ENSO characteristics in a coupled model. *Clim. Dyn.*, **39**,
655 681-707, doi: 10.1007/s00382-011-1247-2.
656 Mo, K. C., and J. N. Paegle, 2001: The Pacific-South American mode and their downstream
657 effects. *Int. J. Climatol.*, **21**, 1211-1229, doi: 10.1002/joc.685.
658 Morioka, Y., T. Tozuka, and T. Yamagata, 2010: Climate variability in the southern Indian
659 Ocean as revealed by self-organizing maps. *Clim. Dyn.*, **35**, 1059-1072, doi:

660 10.1007/s00382-010-0843-x.
661 Morioka, Y., T. Tozuka, and T. Yamagata, 2011: On the growth and decay of the subtropical
662 dipole mode in the South Atlantic. *J. Climate*, **24**, 5538-5554, doi:
663 10.1175/2011JCLI4010.1.
664 Morioka, Y., T. Tozuka, S. Masson, P. Terray, J. J. Luo, and T. Yamagata, 2012: Subtropical
665 dipole modes simulated in a coupled general circulation model. *J. Climate*, **25**,
666 4029-4047, doi: 10.1175/JCLI-D-11-00396.1.
667 Morioka, Y., T. Tozuka, and T. Yamagata, 2013a: How is the Indian Ocean Subtropical
668 Dipole excited? *Clim. Dyn.*, **41**, 1955-1968, doi: 10.1007/s00382-012-1584-9.
669 Morioka, Y., J. V. Ratnam, W. Sasaki, and Y. Masumoto, 2013b: Generation mechanism of
670 the South Pacific subtropical dipole. *J. Climate*, **26**, 6033-6045, doi:
671 10.1175/JCLI-D-12-00648.1.
672 North, G. R., T. L. Bell, R. F. Cahalan, and F. J. Moeng, 1982: Sampling errors in the
673 estimation of empirical orthogonal functions. *Mon. Wea. Rev.*, **110**, 699-706.
674 Raphael, M. N., 2003: Impact of observed sea-ice concentration on the Southern Hemisphere
675 extratropical atmospheric circulation in summer. *J. Geophys. Res.*, **108**, D22, 4687,
676 doi: 10.1029/2002JD003308.
677 Rayner, N. A., D. E. Parker, E. B. Horton, C. K. Folland, L. V. Alexander, D. P. Rowell, E. C.
678 Kent, and A. Kaplan, 2003: Global analyses of sea surface temperature, sea ice, and
679 night marine air temperature since the late nineteenth century. *J. Geophys. Res.*, **108**,
680 D14, 4407, doi: 10.1029/2002JD002670.
681 Reason, C. J. C., 2001: Subtropical Indian Ocean SST dipole events and southern African

682 rainfall. *Geophy. Res. Lett.*, **28**, 2225-2227.
683 Reynolds, R. W., N. A. Rayner, T. M. Smith, D. C. Stokes, and W. Wang, 2002: An improved
684 in situ and satellite SST analysis for climate. *J. Climate*, **15**, 1609-1625.
685 Reynolds, R. W., T. M. Smith, C. Liu, D. B. Chelton, K. S. Casey, and M. G. Schlax, 2007:
686 Daily high-resolution blended analyses for sea surface temperature. *J. Climate*, **20**,
687 5473-5496, doi: 10.1175/2007JCLI1824.1.
688 Richard, Y., S. Trzaska, P. Roucou, and M Rouault, 2000: Modification of the southern
689 African rainfall variability/ENSO relationship since the late 1960s. *Clim. Dyn.*, **16**,
690 883-895.
691 Robertson, A. W., J. D. Farrara, and C. R. Mechoso, 2003: Simulations of the atmospheric
692 response to South Atlantic sea surface temperature anomalies. *J. Climate*, **16**,
693 2540-2551.
694 Roeckner, E., and Coauthors, 2003: The atmospheric general circulation model ECHAM5:
695 Part I: model description. Max-Planck-Institut für Meteorologie, Hamburg,
696 MPI-Report 349.
697 Saji, N. H., B. N. Goswami, P. N. Vinayachandran, and T. Yamagata, 1999: A dipole mode in
698 the tropical Indian Ocean. *Nature*, **401**, 360-363.
699 Santoso, A., M. H. England, and W. Cai, 2012: Impact of Indo-Pacific feedback interactions
700 on ENSO dynamics diagnosed using ensemble climate simulations. *J. Climate*, **25**,
701 7743-7763.
702 Saravanan, R., and P. Chang, 2000: Interaction between tropical Atlantic variability and El
703 Niño-Southern Oscillation. *J. Climate*, **13**, 2177-2194.

704 Screen J. A., N. P. Gillett, A. Y. Karpechko, and D. P. Stevens, 2010: Mixed layer
705 temperature response to the Southern Annular Mode: mechanisms and model
706 representation. *J. Climate*, **23**, 664-678, doi: 10.1175/2009JCLI2976.1.
707 Sen Gupta, A. and M. H. England, 2006: Coupled ocean-atmosphere-ice response to
708 variations in the Southern Annular mode. *J. Climate*, **19**, 4457-4486.
709 Sen Gupta, A. and M. H. England, 2007: Coupled ocean-atmosphere feedback in the Southern
710 Annular Mode. *J. Climate*, **20**, 3677-3692, doi: 10.1175/JCLI4200.1.
711 Sexton, D. M. H., 2001: The effect of stratospheric ozone depletion on the phase of the
712 Antarctic Oscillation. *Geophy. Res. Lett.*, **28**, 3697-3700.
713 Simmonds, I., and W. F. Budd, 1991: Sensitivity of the Southern Hemisphere circulation to
714 leads in the Antarctic pack ice. *Q. J. R. Meteorol. Soc.*, **117**, 1003-1024.
715 Smith, T.M., R.W. Reynolds, T. C. Peterson, and J. Lawrimore, 2008: Improvements to
716 NOAA's historical merged land-ocean surface temperature analysis (1880-2006). *J.*
717 *Climate*, **21**, 2283-2296.
718 Suzuki, R., S. K. Behera, S. Iizuka, T. Yamagata, 2004: Indian Ocean subtropical dipole
719 simulated using a coupled general circulation model. *J. Geophys. Res.*, **109**, C09001,
720 doi: 10.1029/2003JC001974.
721 Takaya, K., and H. Nakamura, 1997: A formulation of a wave-activity flux for stationary
722 Rossby waves on a zonally varying basic flow. *Geophys. Res. Lett.*, **24**, 2985-2988.
723 Takaya, K., and H. Nakamura, 2001: A formulation of a phase-independent wave-activity
724 flux for stationary and migratory quasigeostrophic eddies on a zonally varying basic
725 flow. *J. Atmos. Sci.*, **58**, 608-627.

726 Thompson, D. W. J., and J. M. Wallace, 2000: Annular modes in the extratropical circulation.
727 Part I: month-to-month variability. *J. Climate*, **13**, 1000-1016.
728 Ummenhofer, C. C., A. S. Gupta, A. S. Taschetto, and M. H. England, 2009: Modulation of
729 Australian precipitation by meridional gradients in East Indian Ocean sea surface
730 temperature. *J. Climate*, **22**, 5597-5610, doi: 10.1175/2009JCLI3021.1.
731 Valcke, S., A. Caubel, R. Vogelsang, and D. Declat, 2004: OASIS3 ocean atmosphere sea ice
732 soil user's guide. *Tech. Rep. TR/CMGC/04/68*, CERFACS, Toulouse, France.
733 Wu, R., and B. P. Kirtman, 2004: Understanding the impacts of the Indian Ocean on ENSO
734 variability in a coupled GCM. *J. Climate*, **17**, 4019-4031.
735 Wang, Y. H., and G. Magnusdottir, 2011: Tropospheric Rossby wave breaking and the SAM.
736 *J. Climate*, **24**, 2134-2146, doi: 10.1175/2010JCLI4009.1.
737 Xie, P, and P. A. Arkin, 1997: Analyses of global monthly precipitation using gauge
738 observations, satellite estimates, and numerical model predictions. *J. Climate*, **9**,
739 840-858.
740 Yamazaki, K., and Y. Sinya, 1999: Analysis of the Arctic Oscillation simulated by AGCM. *J.*
741 *Meteor. Soc. Japan*, **77**, 1287-1298.
742 Yu, J. Y., C. R. Mechoso, J. C. McWilliams, and A. Arakawa, 2002: Impacts of the Indian
743 Ocean on the ENSO cycle. *Geophys. Res. Lett.,* **29**, doi: 10.1029/2001GL014098
744 Yuan, C., T. Tozuka, J. J. Luo, and T. Yamagata, 2013: Predictability of the subtropical
745 dipole modes in a coupled ocean-atmosphere model. *Clim. Dyn.*, doi:
746 10.1007/s00382-013-1704-1.
747 Zebiak, S. E., 1993: Air-sea interaction in the equatorial Atlantic region. *J. Climate*, **6**,

748 1567-1586.

749

Tables

Table 1: (a) Details of CGCM experiments performed in this study. (b) EOF modes of SST anomalies in each subtropical-to-midlatitude oceanic basin to define the IOSD, SASD, and SPSD for the observation (OISST) and CGCM (CTR, FTP, FTIO, and FTA) experiments. (c) Explained variances (in %) for the corresponding EOF mode in (b).

(a) CGCM experiments

	SST nudging area	Analysis period
CTR	None	80 yr
FTP	Tropical Pacific (30°S-30°N)	30 yr
FTIO	Tropical Indian (30°S-30°N)	30 yr
FTA	Tropical Atlantic (30°S-30°N)	30 yr

(b) EOF mode

	OISST	CTR	FTP	FTIO	FTA
IOSD	2	1	1		1
SASD	1	1	1	1	
SPSD	2	2		3	2

(c) Explained variance %

	OISST	CTR	FTP	FTIO	FTA
IOSD	14.2	24.5	20.8		25.8
SASD	20.6	19.0	23.1	21.5	
SPSD	13.2	11.8		11.1	12.3

Table 2: Observed event years for the IOSD, SASD, and SPSD. Pos (Neg) corresponds to positive (negative) events.

Event years

	IOSD
Pos	1986, 1987, 1992, 1998, 2003, 2005, 2006, 2010
Neg	1982, 1989, 1991, 1995, 1999, 2002
	SASD
Pos	1989, 1996, 1999, 2001, 2008, 2010
Neg	1982, 1987, 1997, 2000, 2002, 2009
	SPSD
Pos	1983, 1984, 1987, 2001, 2003, 2005, 2008
Neg	1986, 1990, 1994, 1997, 2009, 2010

762 **Table 3:** Occurrence frequency (in %) of the IOSD, SASD, and SPSD for the observation
763 (OISST) and CGCM (CTR, FTP, FTIO, and FTA) experiments. Both the positive and
764 negative events are counted together. The values in the parenthesis of the CTR experiment
765 indicate one standard deviation calculated from 50 different sets of 30-yr outputs.

Occurrence frequency %

	OISST	CTR	FTP	FTIO	FTA
IOSD	48.3	50.6 (±5.8)	48.3		51.7
SASD	41.4	50.6 (±6.2)	58.6	48.3	
SPSD	44.8	49.4 (±10.3)		58.6	55.2

766
767

768 **Table 4:** Correlation coefficients among the IOSD, SASD, and SPSD indices during
769 Dec.-Feb. and the AAO index during Nov.-Jan. for the NCEP Reanalysis-2 (NCEP2) data and
770 CGCM (CTR, FTP, FTIO, and FTA) experiments. The asterisk indicates a correlation
771 coefficient exceeding 90 % (95 %) confidence level by the two-tailed t-test for the NCEP2
772 and FTP, FTIO, and FTA experiments (CTR experiment).

Correlation with AAO

	NCEP2	CTR	FTP	FTIO	FTA
IOSD	0.16	0.45*	0.72*		0.54*
SASD	0.67*	0.39*	-0.28	-0.17	
SPSD	0.22	-0.22		-0.42*	-0.60*

773
774
775

Figure captions

Figure 1: Standard deviation (in ºC) of SST anomalies during austral summer for (a) the observation (OISST) and (b) the CGCM CTR experiment. (c-e) As in (b), but for the FTP, FTIO, and FTA experiments, respectively.

Figure 2: (a) Spatial patterns (in ºC) of the EOF modes for the IOSD defined in Table 1b. (b-c) As in (a), but for the SASD and SPSD, respectively. Positive values are shaded.

Figure 3: (a) Monthly standard deviation of the principal component of the corresponding EOF modes for the IOSD defined in Table 1b. The red shade in the CTR experiment indicates one standard deviation calculated from 50 different sets of 30-yr outputs. (b-c) As in (a), but for the SASD and SPSD, respectively.

Figure 4: (a) Composite anomalies of SST (in ºC) during austral summer of the positive IOSD for the observation (OISST) and CGCM (CTR, FTP, and FTA) experiments. (b) As in (a), but for the SLP (in hPa) during Nov.(0)-Jan.(1). For comparison, NCEP Reanalysis-2 (NCEP2) are shown. Anomalies exceeding the 90% (95%) confidence level by two-tailed t-test are shown for the observation, FTP, and FTA experiments (CTR experiment).

Figure 5: Spatial patterns of the first EOF mode of the geopotential height anomalies at 250 hPa (contour interval is 10 m). The NCEP Reanalysis-2 (NCEP2), the CGCM (CTR, FTP, FTIO, and FTA) experiments are shown, respectively. The positive values are shaded. Values on the top of the panel indicate the explained variance.

Figure 6: (a) As in Fig. 4b, but for the geopotential height at 250 hPa (color, in m) and wave activity flux (arrow, in $m^2\ s^{-2}$). (b) As in (a), but for the velocity potential at 250 hPa (color, in $10^6\ m^2\ s^{-1}$) and divergent wind (arrow, in $m\ s^{-1}$).

798 **Figure 7:** As in Fig. 4b, but for the rainfall (color, in mm month^{-1}).

799 **Figure 8:** As in Fig. 4, but for the positive SASD. The FTP and FTIO experiments are shown.

800 **Figure 9:** As in Fig. 6, but for the positive SASD. The FTP and FTIO experiments are shown.

801 **Figure 10:** As in Fig. 7, but for the positive SASD. The FTP and FTIO experiments are
802 shown.

803 **Figure 11:** As in Fig. 4, but for the positive SPSD. The FTIO and FTA experiments are
804 shown.

805 **Figure 12:** As in Fig. 6, but for the positive SPSD. The FTIO and FTA experiments are
806 shown.

807 **Figure 13:** As in Fig. 7, but for the positive SPSD. The FTIO and FTA experiments are
808 shown.

809 **Figure 14:** Schematic diagram illustrating the generation mechanism of the IOSD, SASD,
810 and SPSD derived from the reanalysis data and the CTR experiment. The warm (cold) color
811 indicates the positive (negative) SST anomalies and the black shade indicates the anomalous
812 wind divergence in the upper troposphere as possible sources of the Rossby waves. The
813 dashed line shows the propagation pathway of the anomalous high (H) and low (L) pressure
814 in the upper troposphere.

815 **Figure 15:** As in Fig. 1, but for (a) geopotential height at 250 hPa (in m) during Nov.-Jan.. (b)
816 As in (a), but for the precipitation (in mm month^{-1}).

817

818

Figures

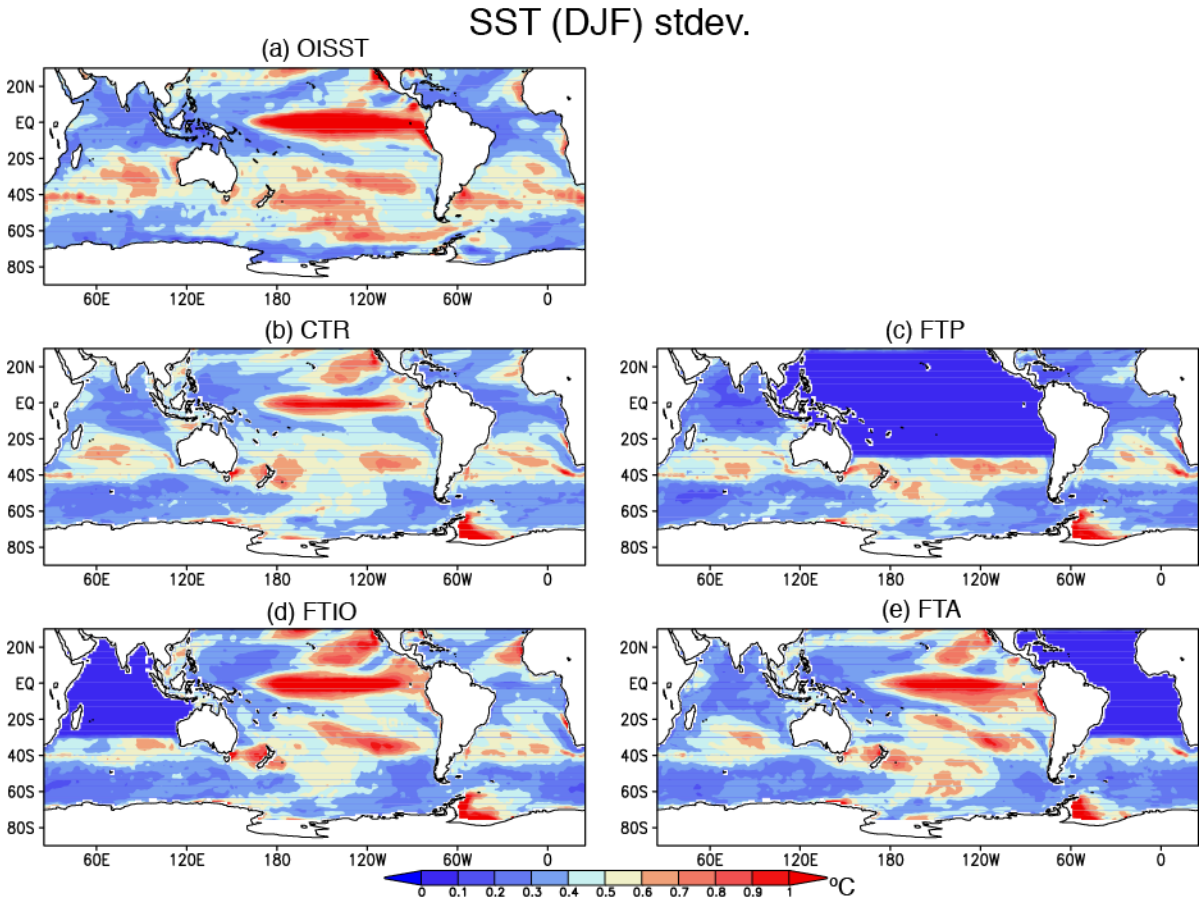

Figure 1: Standard deviation (in ºC) of SST anomalies during austral summer for (a) the observation (OISST) and (b) the CGCM CTR experiment. (c-e) As in (b), but for the FTP, FTIO, and FTA experiments, respectively.

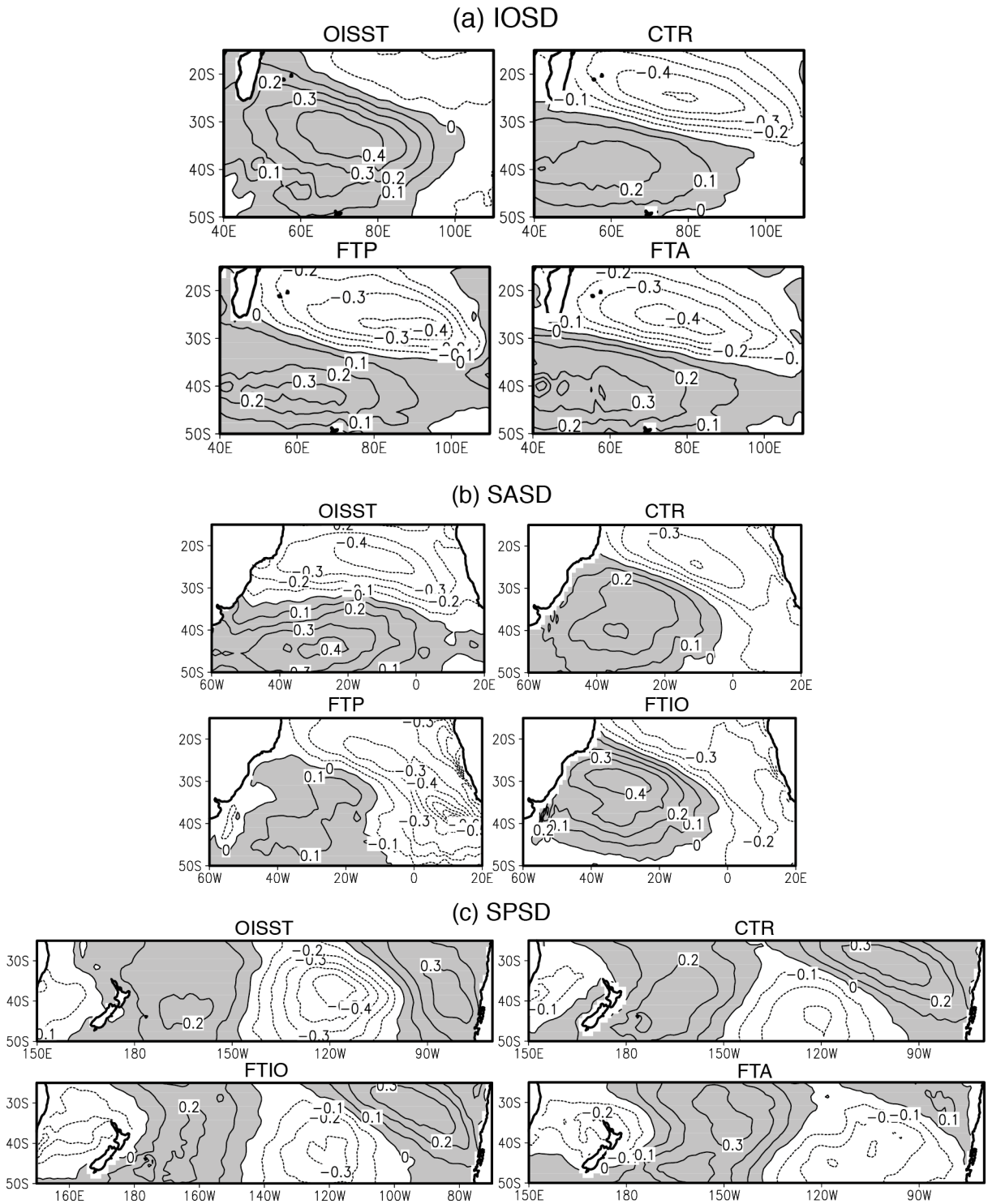

825

826

827

828 **Figure 2:** (a) Spatial patterns (in ºC) of the EOF modes for the IOSD defined in Table 1b.

829 (b-c) As in (a), but for the SASD and SPSD, respectively. Positive values are shaded.

830

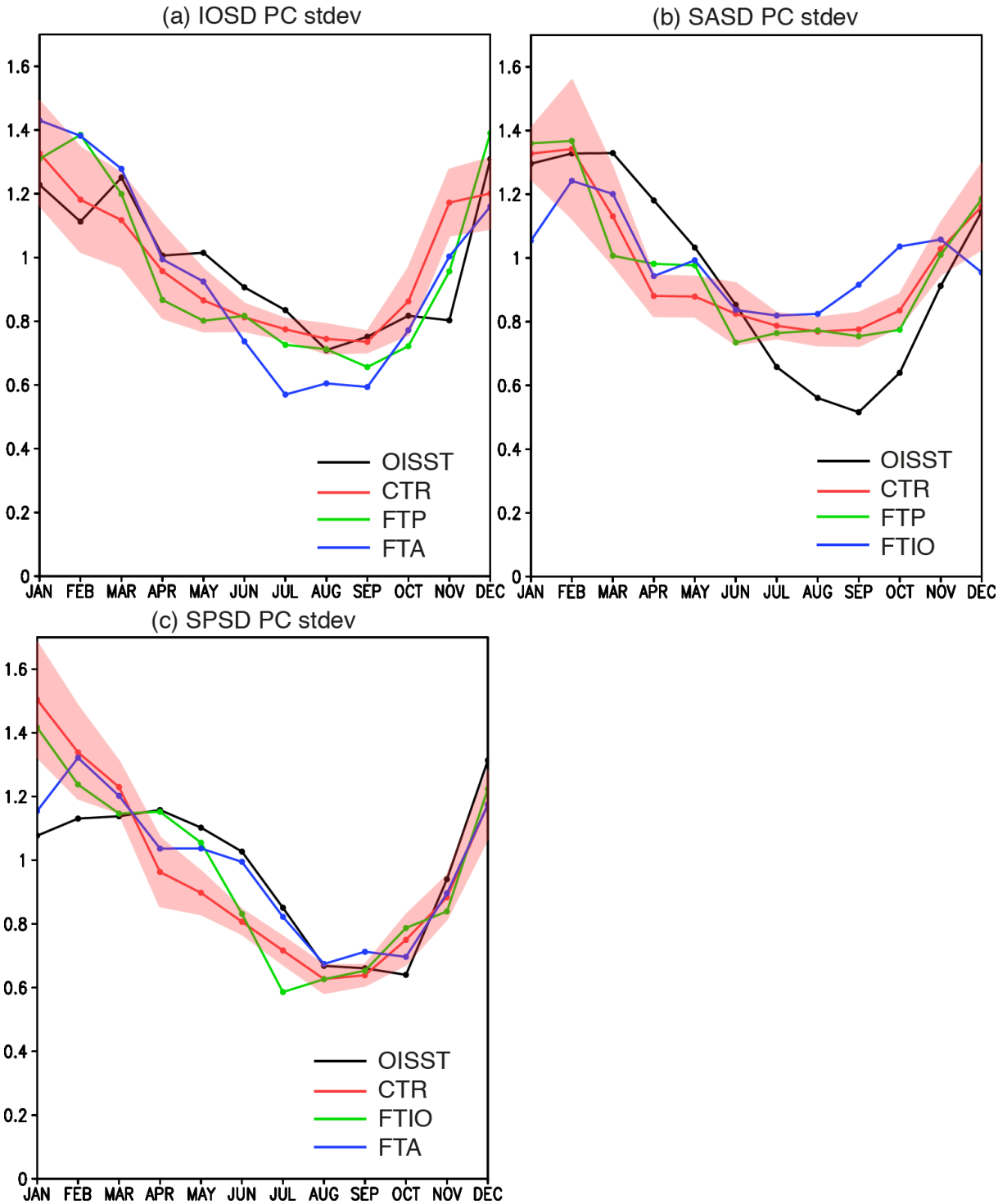

Figure 3: (a) Monthly standard deviation of the principal component of the corresponding EOF modes for the IOSD defined in Table 1b. The red shade in the CTR experiment indicates one standard deviation calculated from 50 different sets of 30-yr outputs. (b-c) As in (a), but for the SASD and SPSD, respectively.

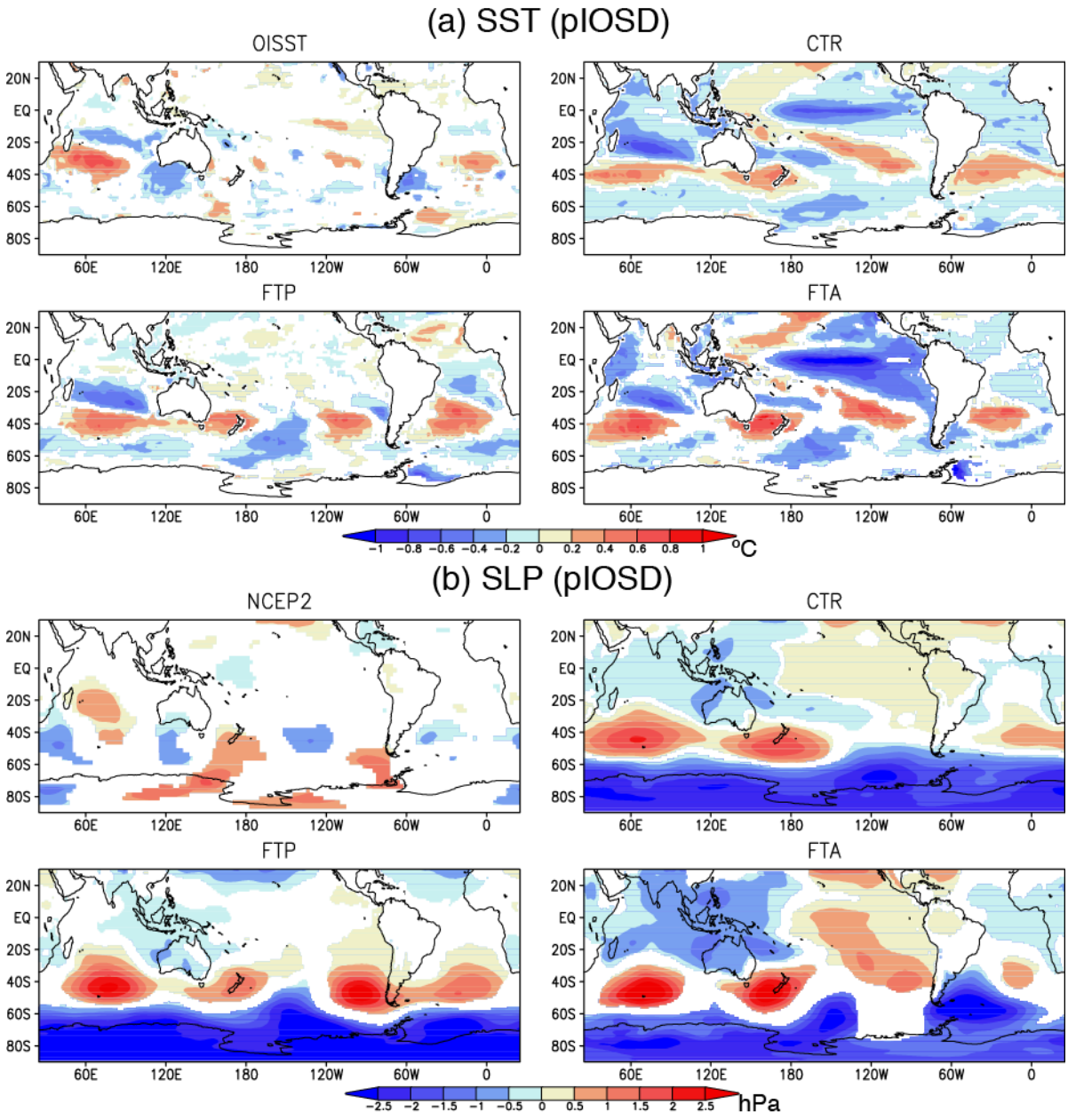

Figure 4: (a) Composite anomalies of SST (in ºC) during austral summer of the positive IOSD for the observation (OISST) and CGCM (CTR, FTP, and FTA) experiments. (b) As in (a), but for the SLP (in hPa) during Nov.(0)-Jan.(1). For comparison, NCEP Reanalysis-2 (NCEP2) are shown. Anomalies exceeding the 90% (95%) confidence level by two-tailed t-test are shown for the observation, FTP, and FTA experiments (CTR experiment).

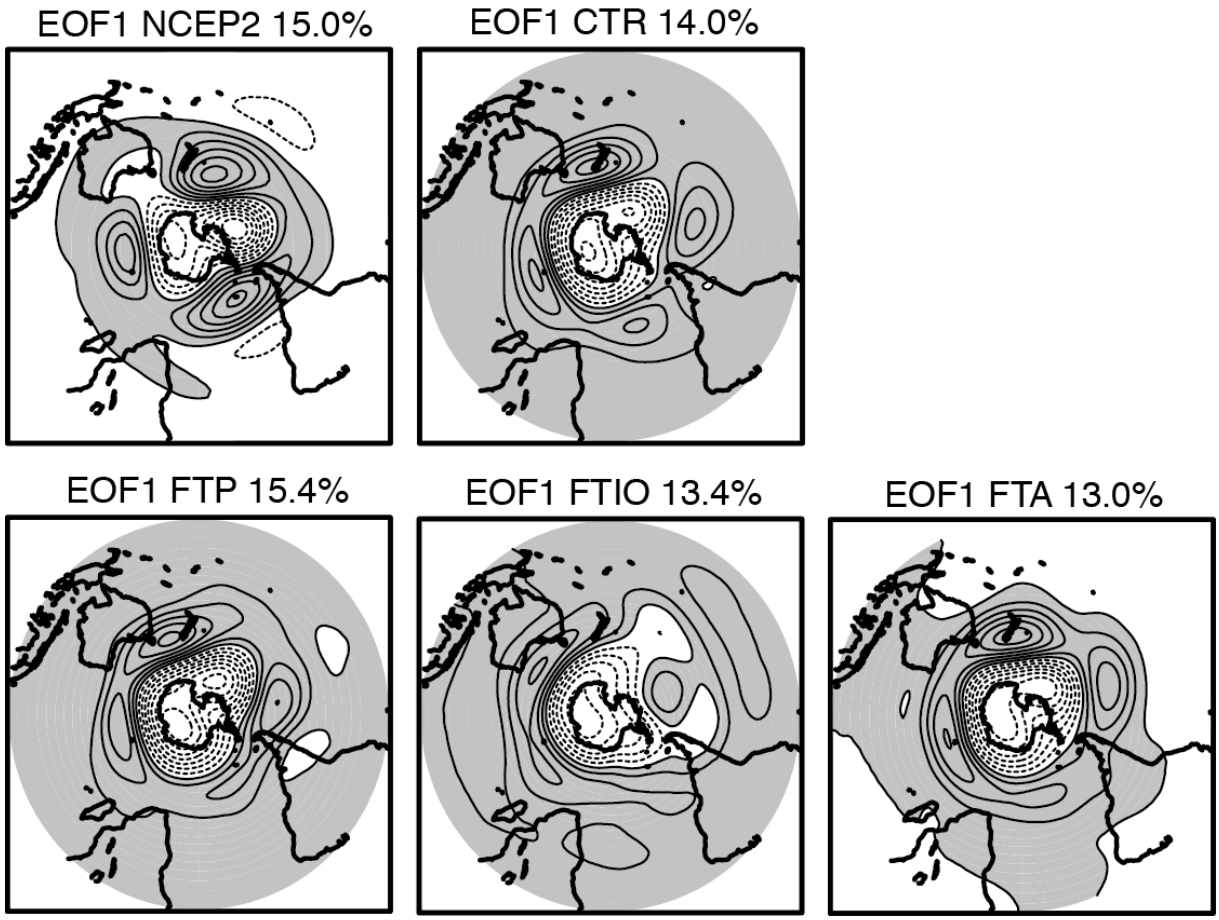

844

845 **Figure 5:** Spatial patterns of the first EOF mode of the geopotential height anomalies at 250
846 hPa (contour interval is 10 m). The NCEP Reanalysis-2 (NCEP2), the CGCM (CTR, FTP,
847 FTIO, and FTA) experiments are shown, respectively. The positive values are shaded.
848 Values on the top of the panel indicate the explained variance.

849

850

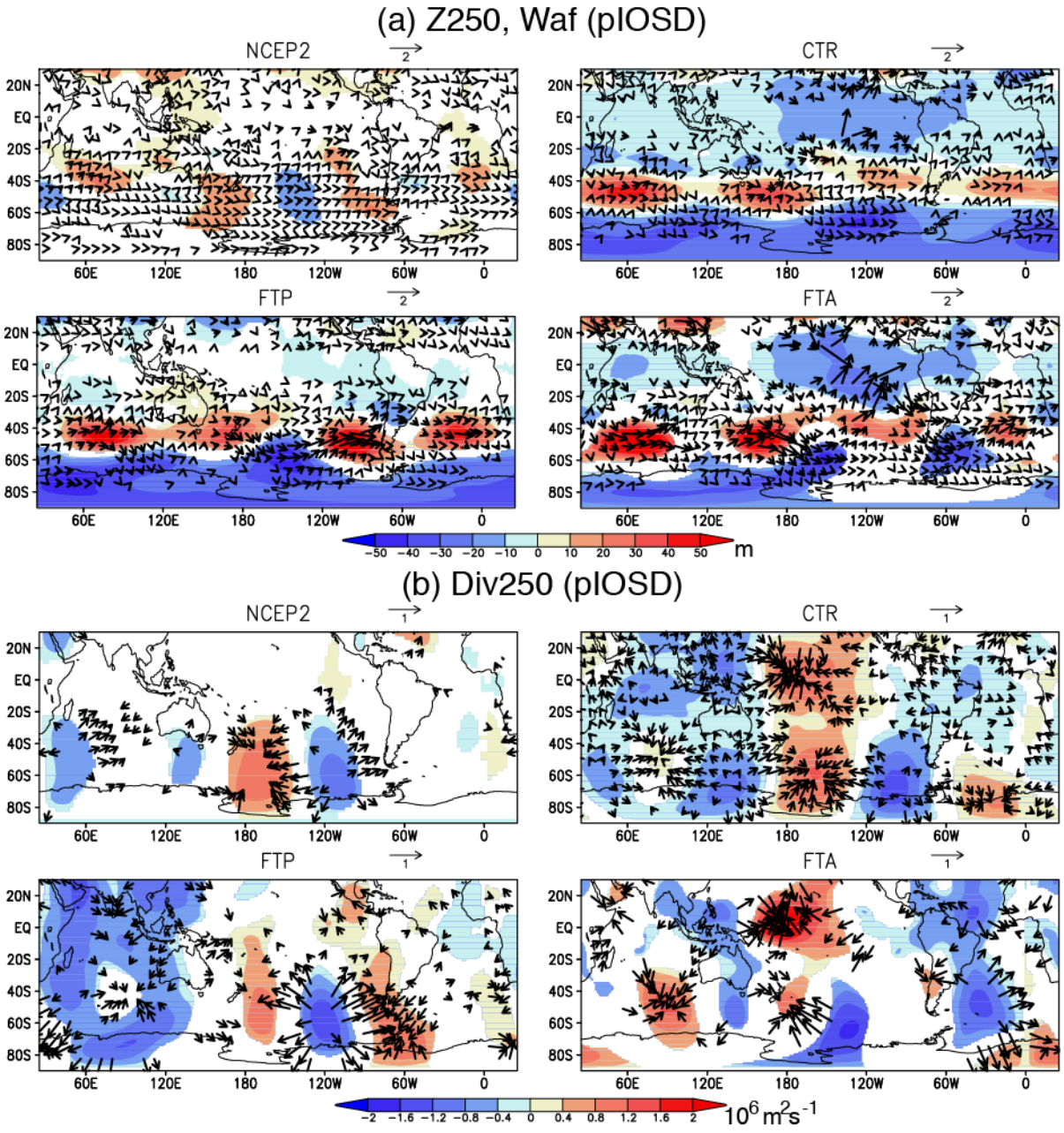

851

852 **Figure 6:** (a) As in Fig. 4b, but for the geopotential height at 250 hPa (color, in m) and wave
853 activity flux (arrow, in $m^2\ s^{-2}$). (b) As in (a), but for the velocity potential at 250 hPa (color, in
854 $10^6\ m^2\ s^{-1}$) and divergent wind (arrow, in $m\ s^{-1}$).

855

856

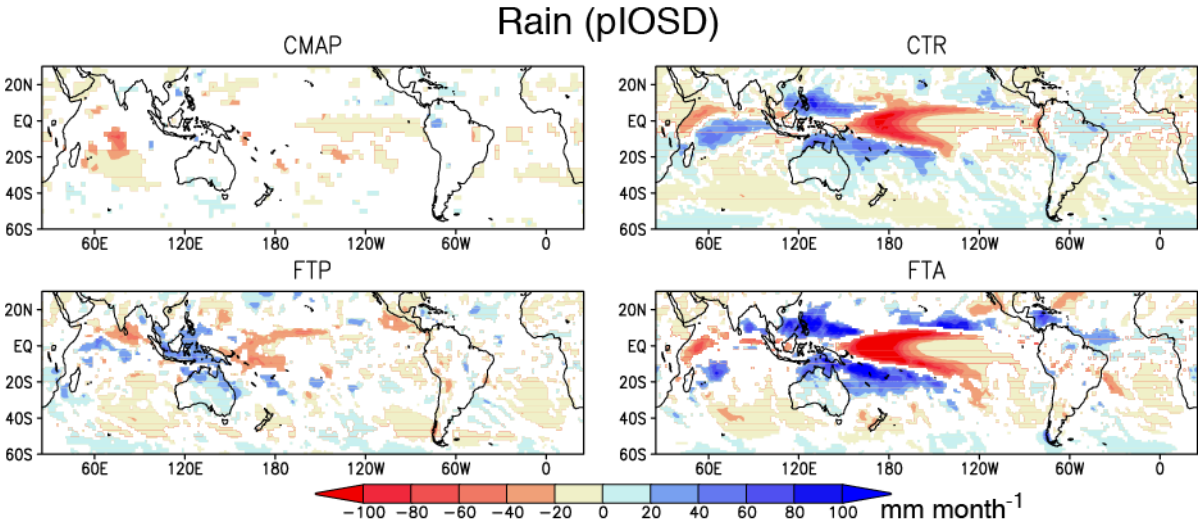

Figure 7: As in Fig. 4b, but for the rainfall (color, in mm month^{-1}).

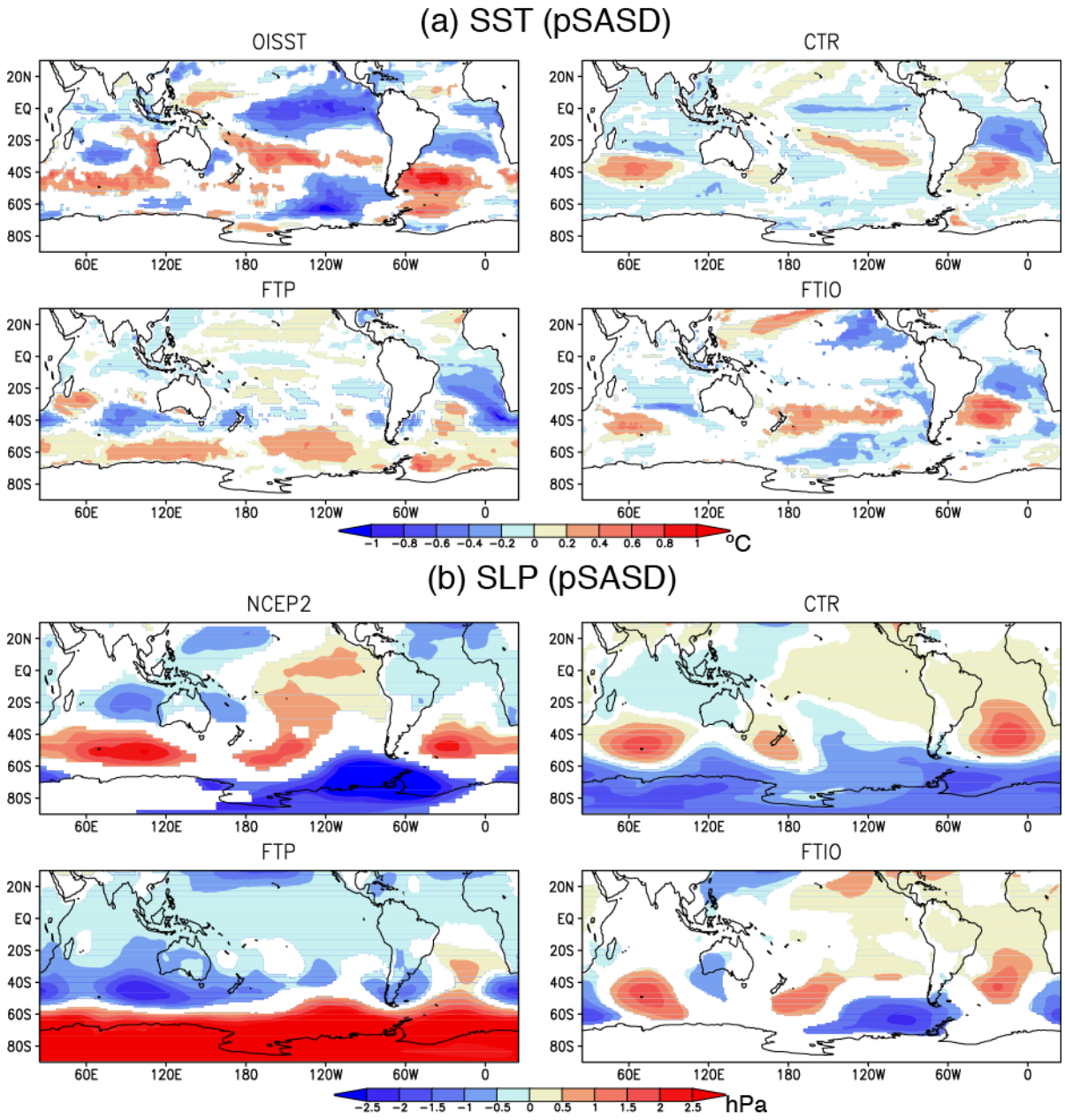

Figure 8: As in Fig. 4, but for the positive SASD. The FTP and FTIO experiments are shown.

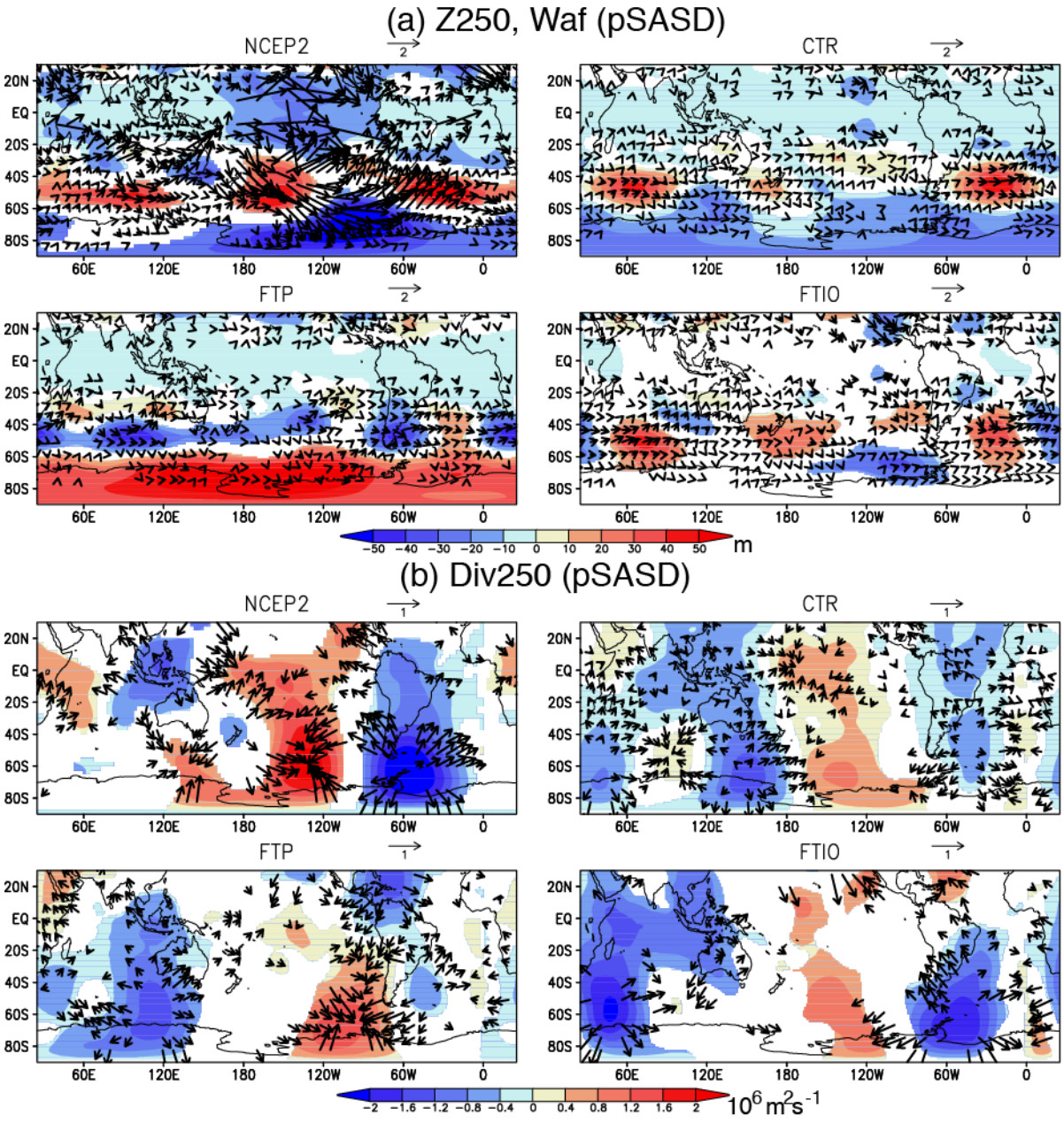

Figure 9: As in Fig. 6, but for the positive SASD. The FTP and FTIO experiments are shown.

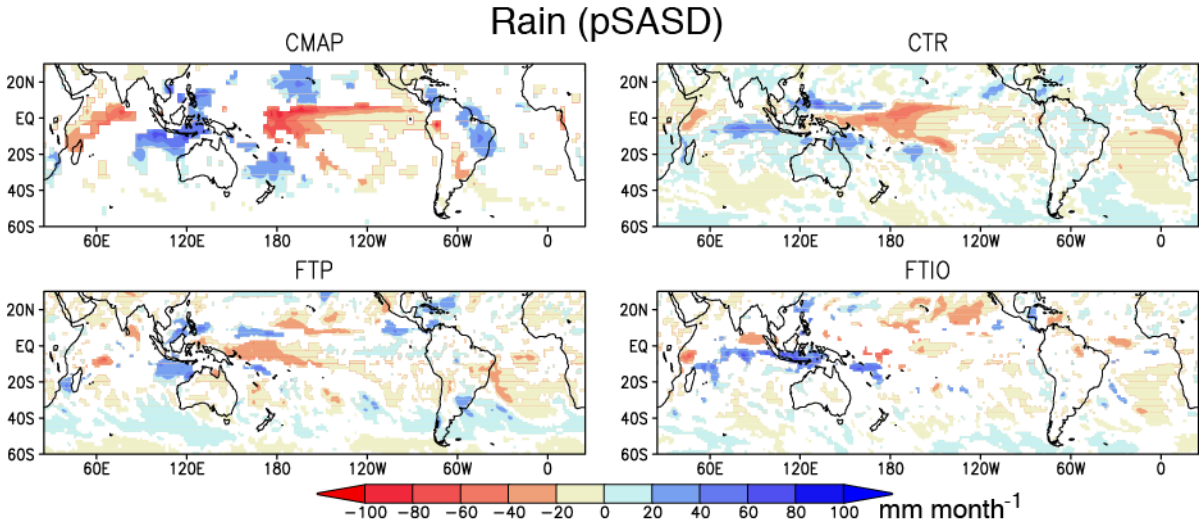

Figure 10: As in Fig. 7, but for the positive SASD. The FTP and FTIO experiments are shown.

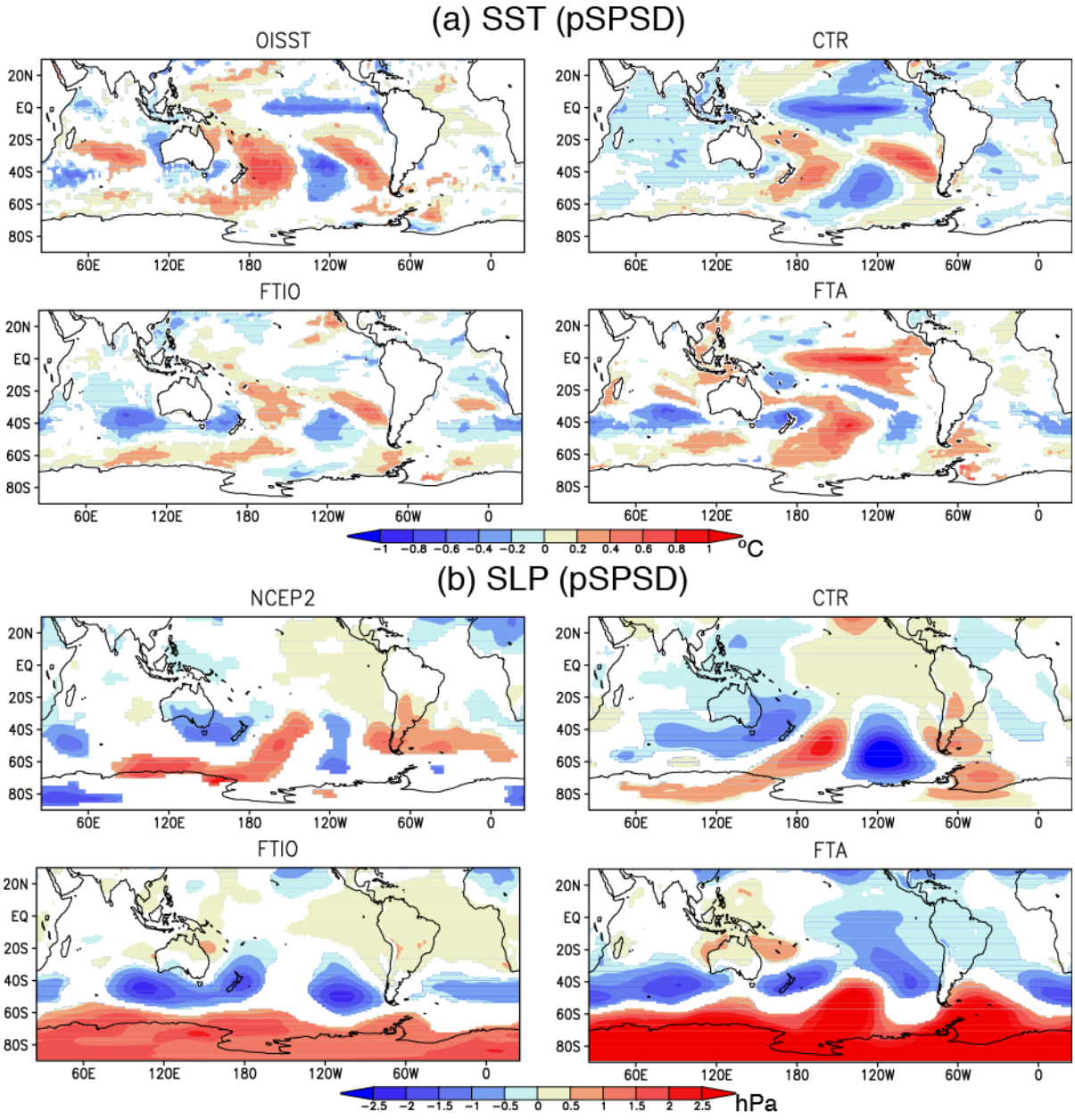

872

873 **Figure 11:** As in Fig. 4, but for the positive SPSD. The FTIO and FTA experiments are

874 shown.

875

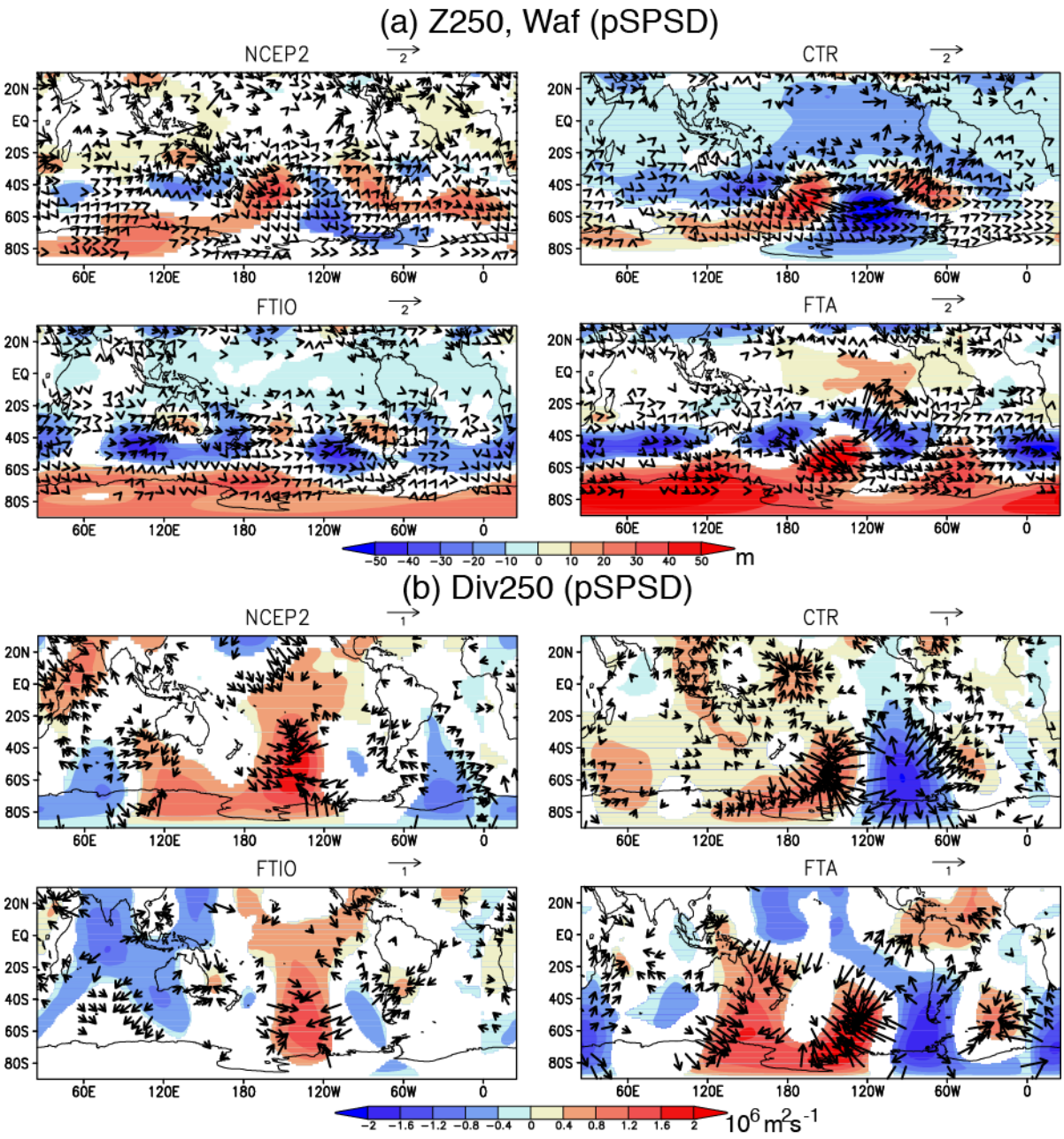

876

877 **Figure 12:** As in Fig. 6, but for the positive SPSD. The FTIO and FTA experiments are

878 shown.

879

880

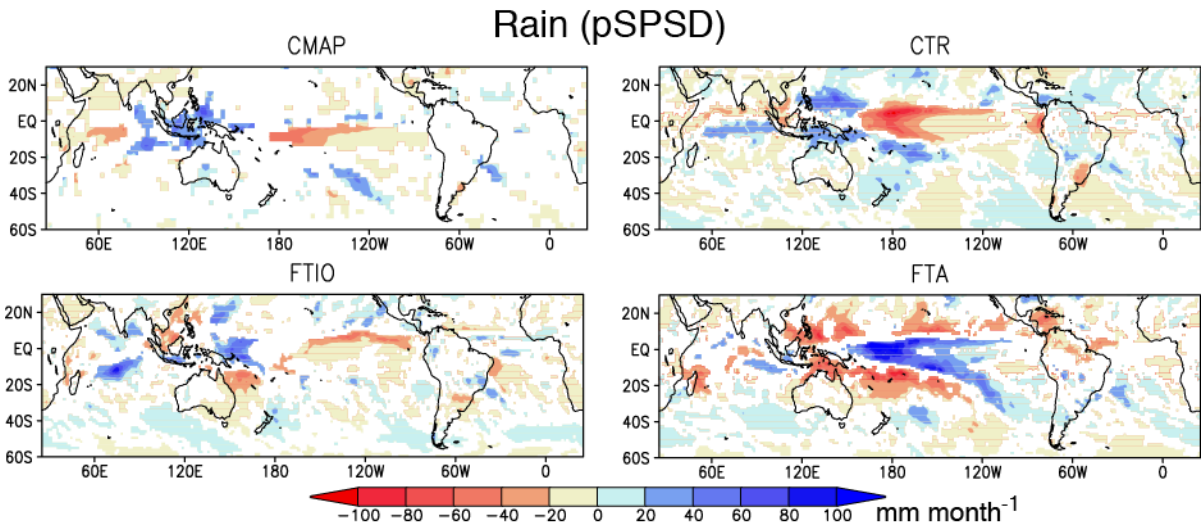

881

882 **Figure 13:** As in Fig. 7, but for the positive SPSD. The FTIO and FTA experiments are

883 shown.

884

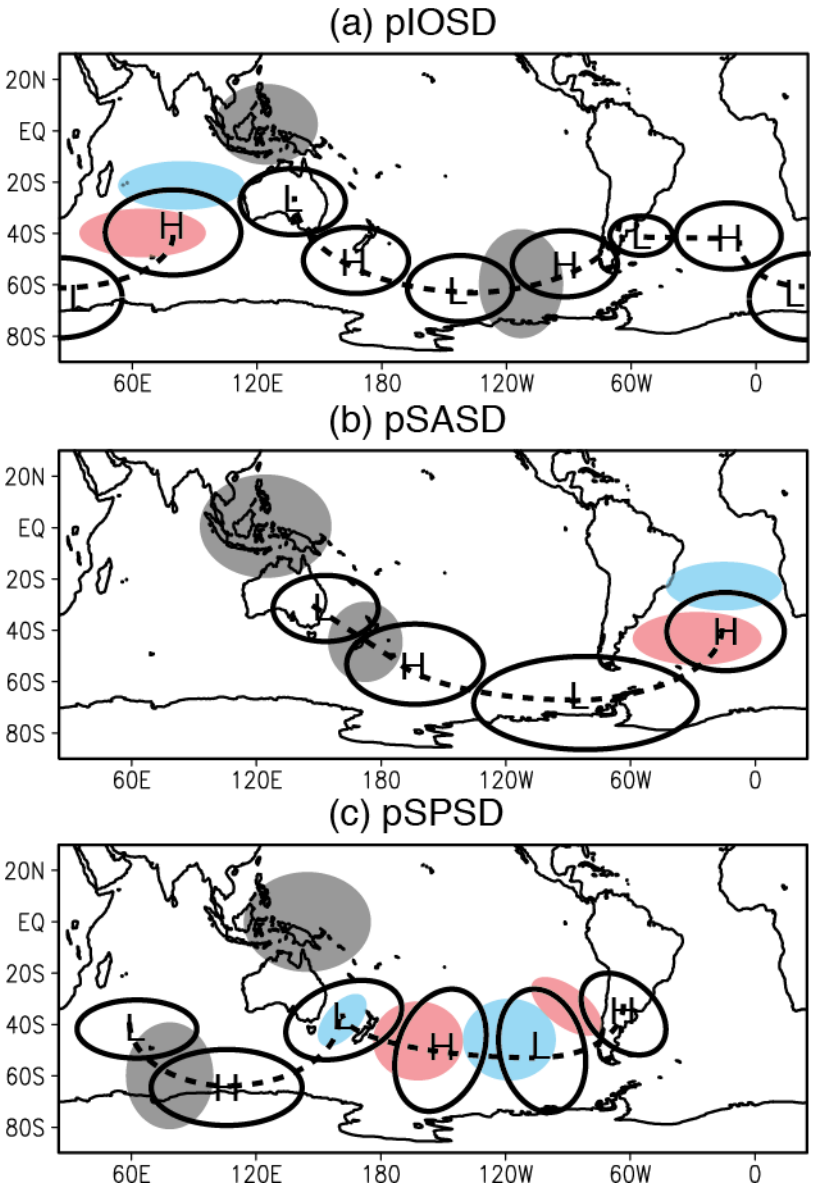

885

886 **Figure 14:** Schematic diagram illustrating the generation mechanism of the IOSD, SASD,
887 and SPSD derived from the reanalysis data and the CTR experiment. The warm (cold) color
888 indicates the positive (negative) SST anomalies and the black shade indicates the anomalous
889 wind divergence in the upper troposphere as potential sources of the Rossby waves. The
890 dashed line shows the propagation pathway of the anomalous high (H) and low (L) pressure
891 in the upper troposphere.

892

893

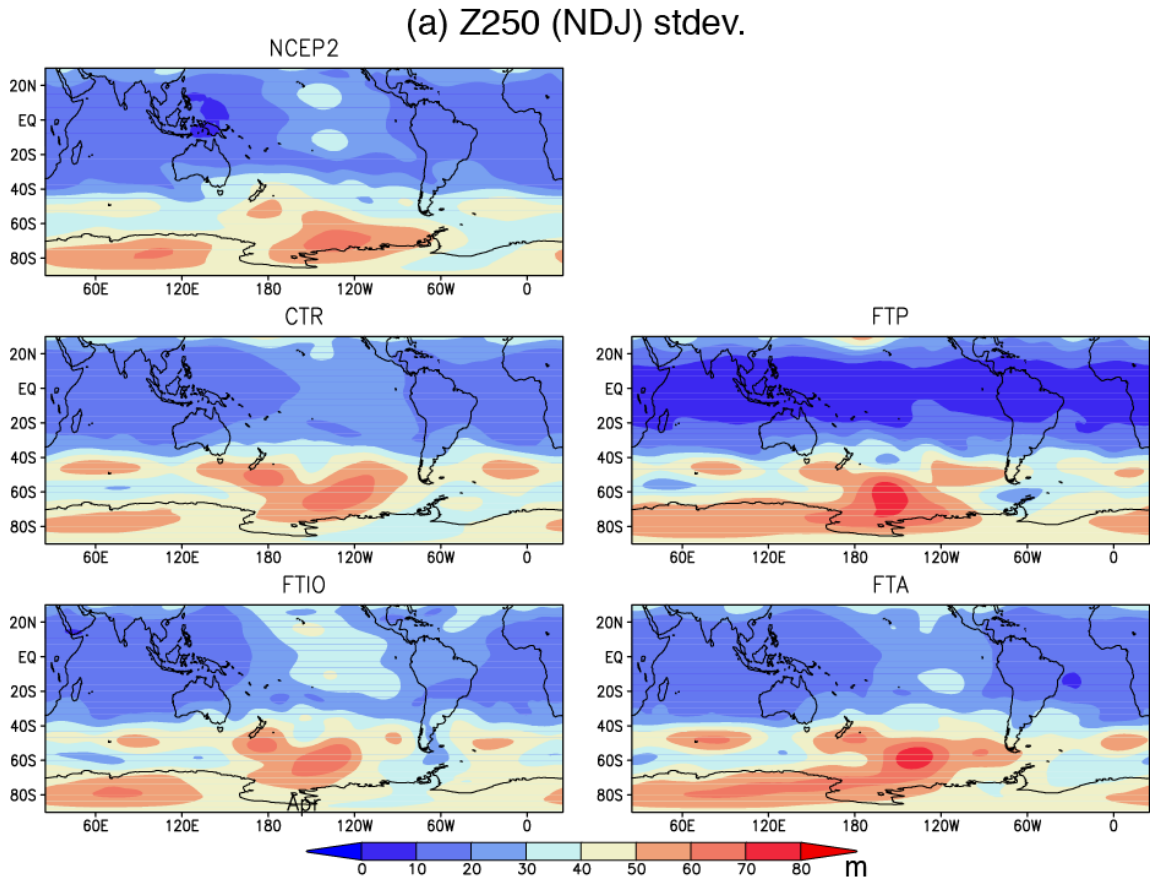

894

895

896 **Figure 15:** As in Fig. 1, but for (a) geopotential height at 250 hPa (in m) during Nov.-Jan.. (b)

897 As in (a), but for the precipitation (in mm month^{-1}).